NOVEL FIBER OPTIC TIP DESIGNS AND DEVICES FOR LASER SURGERY

by

Thomas Clifton Hutchens

A dissertation submitted to the faculty of
The University of North Carolina at Charlotte
in partial fulfillment of the requirements
for the degree of Doctor of Philosophy in
Optical Science and Engineering

Charlotte

2013

Approved by:

____
Dr. Nathaniel M. Fried

____
Dr. Angela D. Davies

____
Dr. M. Yasin A. Raja

____
Dr. Michael A. Fiddy

____
Dr. Christopher J. Evans

ABSTRACT

THOMAS CLIFTON HUTCHENS. Novel fiber optic tip designs and devices for laser surgery. (Under the direction of DR. NATHANIEL M. FRIED)

Fiber optic delivery of laser energy has been used for years in various types of surgical procedures in the human body. Optical energy provides several benefits over electrical or mechanical surgery, including the ability to selectively target specific tissue types while preserving others. Specialty fiber optic tips have also been introduced to further customize delivery of laser energy to the tissue. Recent evolution in lasers and miniaturization has opened up opportunities for many novel surgical techniques.

Currently, ophthalmic surgeons use relatively invasive mechanical tools to dissect retinal deposits which occur in proliferative diabetic retinopathy. By using the tight focusing properties of microspheres combined with the short optical penetration depth of the Erbium:YAG laser and mid-IR fiber delivery, a precise laser scalpel can be constructed as an alternative, less invasive and more precise approach to this surgery. Chains of microspheres may allow for a self limiting ablation depth of approximately 10 μm based on the defocusing of paraxial rays. The microsphere laser scalpel may also be integrated with other surgical instruments to reduce the total number of handpieces for the surgeon.

In current clinical laser lithotripsy procedures, poor input coupling of the Holmium:YAG laser energy frequently damages and requires discarding of the optical fiber. However, recent stone ablation studies with the Thulium fiber laser have provided comparable results to the Ho:YAG laser. The improved spatial beam profile of the Thulium fiber laser can also be efficiently coupled into a fiber approximately one third the diameter and reduces the risk of damaging the fiber input. For this reason, the trunk optical fiber minus the distal fiber tip can be preserved between procedures. The distal fiber tip, which degrades during stone ablation, could be made detachable and disposable. A novel, low-profile, twist-locking, detachable distal fiber tip interface was designed, assembled, and tested for use in Thulium fiber laser lithotripsy. A 1.00-mm-outer-diameter detachable fiber tip interface was designed, constructed, and tested *ex vivo* on urinary stones in the laboratory. Similar stone ablation rates between the previously studied tapered distal fiber tip and the detachable fiber tip were measured. For urologists desiring faster TFL lithotripsy procedures, the incorporation of detachable distal fiber tips allows for rapid replacement of damaged fiber tips without concern about the laser to trunk fiber connection. This method for preserving the trunk fiber could be a motivation for integrating a dedicated laser fiber into the ureteroscope, with detachable distal tips, thus freeing the working channel for the use of other surgical instruments.

During laser lithotripsy, distal fiber tip degradation increases as the fiber core diameter decreases. However, smaller fiber diameters ($\leq 200\ \mu m$) are more desirable because of increased saline irrigation rates in the single working channel of the ureteroscope and less impact on ureteroscope deflection. A hollow fiber cap is proposed to reduced fiber tip degradation in small diameter fibers, without compromising stone ablation rates. The disadvantage of the hollow fiber tip observed in the study is the increase in stone retropulsion. However, integrating the hollow fiber tip with a clinically used stone basket may allow for a robust stone ablation instrument that also minimizes retropulsion. These surgical approaches involving novel specialty fiber optic tip designs are discussed in this thesis.

DEDICATION

I dedicate this dissertation to my parents, Tim and Aprile Hutchens, who have always supported me in each step of my life.

ACKNOWLEDGMENTS

I would like to thank Dr. Nathaniel Fried, my advisor, for his continued support and guidance through my research and academic studies. I would also like to thank Dr. Angela Davies for building my interest in optics and encouraging me to enroll in the Optical Science and Engineering program as well as for offering me my first research opportunity. I appreciate the assistance of my other committee members as well in critiquing and steering my thesis topic and content in the right direction. I also appreciate the Graduate Assistant Support Plan (GASP) provided by the graduate school at UNC Charlotte.

I would like to thank all of my fellow Biomedical Optics Laboratory members and members of other laboratories that have provided insight and assistance throughout my graduate career: Dr. Christopher Cilip, Dr. Serhat Tozburun, Dr. Richard Blackmon, Dr. Shahab Chitchian, Sarah Rosenbury, Gino Schweinsberger, Charlotte Stahl, Nicholas Giglio, William Perkins, Arash Darafsheh, Stephen Burand, Kenneth Allen, Jason Case, Benrui Zheng, Yue Dong, Scott Williams, Dr. Awad Gerges, and Dr. Vasily Astratov.

The research for the ophthalmic scalpel project was supported by the National Institutes of Health (Grant#R41EY019598). I would like to thank Cliff Williams and Mike Quinn from Carolinas Medical Center for providing the porcine eyes, and Eric Smith from Celligent Technologies for processing the tissue samples for histology. Dr. Vasily Astratov and the Mesophotonics Lab provided microsphere handling and measurement equipment as well as valuable insight into theory and characterization methods. Dr. Howard Ying, ophthalmologist at John Hopkins Medical Center, provided guidance in tissue dissection and integration methods for the microsphere scalpel.

I would like to thank Dr. Pierce Irby, Director of the Carolinas Kidney Stone Center and a urologist at Carolinas Medical Center, for helpful discussions on laser lithotripsy and novel endoscope designs. I would also like to thank Dr. Christopher Evans and his students, Katelyn Bernasconi and Eric Browy, from the UNC Charlotte Center for Precision Metrology, for providing assistance in operating the scanning white light interferometer supplied by Zygo Corporation.

TABLE OF CONTENTS

LIST OF TABLES xii

LIST OF FIGURES xiii

LIST OF ABBREVIATIONS xvii

CHAPTER 1: INTRODUCTION 1

CHAPTER 2: OPHTHALMIC MICROSPHERE LASER SCALPEL 2

- 2.1: Background and Overview 2
  - 2.1.1: Current Ophthalmic Surgical Techniques 2
  - 2.1.2: Erbium:YAG Laser for Tissue Ablation 3
  - 2.1.3: Surgical Laser Microprobes and Microspheres 4
- 2.2: Design and Testing of Microsphere Scalpel 6
  - 2.2.1: Laser Source and Fiber Delivery 6
  - 2.2.2: Microsphere Scalpel Design 6
  - 2.2.3: Microsphere Scalpel Construction 8
  - 2.2.4: Experimental Tissue Setup 9
- 2.3: Results 10
  - 2.3.1: Microsphere Scalpel Characterization 10
  - 2.3.2: Ablation Crater Measurements on Corneal Tissue 11
- 2.4: Discussion 14
  - 2.4.1: Uncertainty in Characterization Results 14
  - 2.4.2: Tissue Results 15
  - 2.4.3: Possible Improvements 17
- 2.5: Conclusions 19

CHAPTER 3: OPTIMIZATION & PACKAGING OF MICROSPHERE SCALPEL 20

- 3.1: Previous *ex vivo* Study 20
- 3.2: Materials and Methods 22
  - 3.2.1: Theoretical Modeling 22
  - 3.2.2: Microsphere Scalpel Detachable Tip with Illumination 24
  - 3.2.3: Experimental Tissue Setup 26
- 3.3: Results and Disscussion 28
  - 3.3.1: Tissue Study 28
  - 3.3.2: Discussion 29
- 3.4: Multifunctional Scalpel 31
- 3.5: Conclusions 33

CHAPTER 4: DETACHABLE FIBER OPTIC TIPS FOR LASER LITHOTRIPSY 34

- 4.1: Background and Overview 34
  - 4.1.1: Current Laser Lithotripsy Techniques 34
  - 4.1.2: Thulium Fiber Laser Lithotripsy 36
  - 4.1.3: Tapered Distal Fiber Tips 39
  - 4.1.4: Detachable Fiber Tips 40
- 4.2: Materials and Methods 42
  - 4.2.1: Laser and Tapered Fiber 42
  - 4.2.2: Detachable Fiber Tip Design 43
  - 4.2.3: Optical and Thermal Characterization 47
  - 4.2.4: Lithotripsy Setup 47
  - 4.2.5: Fiber Tip Degradation 49

4.3: Results 50

4.3.1: Optical and Thermal Measurements 50

4.3.2: Lithotripsy 52

4.3.3: Fiber Tip Degradation 53

4.4: Discussion 56

4.4.1: Detachable Fiber Tip Design 56

4.4.2: Optical and Thermal Analysis 56

4.4.3: Lithotripsy Analysis 58

4.4.4: Degradation Analysis 59

4.5: Conclusions 61

CHAPTER 5: HOLLOW FIBER TIPS FOR LASER LITHOTRIPSY 62

5.1: Background 62

5.1.1: Motivation for Hollow Fiber Tips 62

5.1.2: Retropulsion and Suction Effect 63

5.2: Materials and Methods 64

5.2.1: Hollow Fiber Tips 64

5.2.2: Retropulsion Study 65

5.2.3: Stone Ablation Study 66

5.2.4: Fiber Burn-back and Degradation 66

5.3: Results 67

5.3.1: Stone Ablation 67

5.3.2: Fiber Tip Degradation 68

5.3.3: Retropulsion 69

5.4: Discussion 70

5.5: Integration with Stone Basket 71

5.6: Fiber Muzzle 72

5.6.1: Theory and Motivation 72

5.6.2: Prototype Testing 73

5.7: Conclusions 75

CHAPTER 6: CONCLUSIONS 76

REFERENCES 78

APPENDIX A: PEER-REVIEWED PUBLICATIONS 84

APPENDIX B: CONFERENCE PROCEEDINGS 85

APPENDIX C: PATENTS 86

APPENDIX D: ASSEMBLY OF GLUED MICROSPHERE SCALPEL 87

APPENDIX E: ASSEMBLY OF LITHOTRIPSY DETACHABLE TIPS 88

LIST OF TABLES

TABLE 2.1: Corneal ablation crater dimensions at pulse energies of 0.1 mJ (S.D. = 10 μm). 12

TABLE 4.1: Materials used to assemble detachable fiber optic tip prototype. All dimensions for inner (ID), outer diameter (OD), and cut length are in millimeters. 45

TABLE 4.2: Peak temperature and temperature rise (°C) of detachable and tapered fiber tips as a function of laser temporal pulse profile. Mean room temperature for detachable (24.6°C) and tapered (24.9°C) fiber measurements. Pulse energy: 30±2 mJ. 50

TABLE 4.3: COM stone ablation rates (μg/s) for detachable and tapered fiber tips as a function of laser pulse rate and profile. Rates calculated from mass loss after 6000 pulses (N=5). Pulse energy: 30±2 mJ. 53

TABLE 4.4: Surface (S) and line profile (R) roughness measurements. Comparison of polished fiber, before and after 60,000 500-μs pulses at a standard pulse rate of 50 Hz with a pulse energy of 30 mJ. All dimensions are in nanometers. 54

TABLE 5.1: COM stone ablation rates and fiber burn-back for the hollow fiber tips as a function of fiber recession. Silica fiber with 150 μm core diameter. Rates calculated from mass loss after 9000 pulses at 150 Hz, 500 μs pulse duration (N≥5). Pulse energy: 34±1 mJ. Uncertainty of 25 μm on burn-back measurements (N≥10). 67

LIST OF FIGURES

FIGURE 2.1: Water absorption data plotted across mid-IR wavelengths. Peak absorption occurs at λ=2940 nm. [24] 4

FIGURE 2.2: Er:YAG normal-spiking mode 75 µs pulse profile. 6

FIGURE 2.3: Proposed ophthalmologic surgical configurations consisting of a 30-mm-long hollow waveguide of 0.75-mm-diameter with microsphere focusing at distal tip. The diameter of a typical human eye is 24 mm [32]. 8

FIGURE 2.4: (top row) Normalized simulation of the intensity measured at the minimum beam waist (FWHM) for one, three, and five sphere configurations. Courtesy of Arash Darafsheh. (bottom row) 3D beam profiles acquired by magnifying the minimum beam waist onto the IR beam profiler's detector array. As the number of spheres increase a reduction in (FWHM) spot diameter and an expanding low intensity mode filtering ring can be seen in both simulation and experiment. 11

FIGURE 2.5: Simulated intensity profiles for one, three, and five sphere probes at minimum spot size occurring at 10 µm after sphere vertex, courtesy of Arash Darafsheh (Top row). Representative bird's eye corneal crater images for one, three, and five sphere probes at 0.1 mJ (Middle row). Representative histology images for one, three, and five sphere probe craters at 0.1 mJ with trichrome stain (Bottom row). Each cell size: 120 x 120 µm. 13

FIGURE 2.6: Beam characterization of the microsphere probe using a NA=0.5 magnification lens to focus the minimum waist onto the infrared beam profiler's detector array 500 mm away. Rays beyond the numerical aperture of the lens were not characterized experimentally but are present in simulations and tissue testing since the device operates in contact mode with tissue. The simulation was performed using FRED. 15

FIGURE 3.1: A focusing microprobe design based on arrays of spheres placed in a hollow waveguide. Courtesy of Arash Darafsheh. 22

FIGURE 3.2: Irradiance distribution for different distances from the tip of a microprobe composed of (a) 1, (b) 3, and (c) 5 spheres with n=1.71. (d) Red rays correspond to PFMs which provide sharp focusing at the surface of every odd number of spheres. Blue rays correspond to paraxial rays. Courtesy of Arash Darafsheh. 24

FIGURE 3.3: Detachable microsphere scalpel with integrated illumination. 25

FIGURE 3.4: Detachable microsphere scalpel prototype compared to two common ocular surgical instruments, each of which are 23 gauge (~625 μm). For the microsphere scalpel, two standard SMA fiber connectors are integrated using a mating sleeve. 26

FIGURE 3.5: Trichrome histology of ablation craters created in epithelium layer of cornea using detachable microsphere scalpel with integrated illumination. 28

FIGURE 3.6: The three possible modalities for microsphere scalpel improvement are shown with an additional illumination probe in a retinopathy surgery configuration. (a) Handpiece. (b) Probe Tip. (c) *Ex vivo* intraocular surgical configuration. (d) Cross-section of retinopathy surgery with multifunctional probes (e) magnified. 32

FIGURE 4.1: Spatial beam waist profiles for (a) Ho:YAG laser (300 μm) on the left, and (b) Thulium fiber laser (70 μm) on the right. Unlike the TFL beam, the multimode Ho:YAG laser beam typically overflows 150 and 200 μm core fibers [37]. 37

FIGURE 4.2: The TFL room temperature water absorption peak at 1940 nm shifts to about 1910 nm at ablation temperatures. The major emission lines of the TFL at 1908 and 1940 nm match this shifting peak more closely than the Ho:YAG laser (2120 nm) [47]. 37

FIGURE 4.3: Tapered fiber distal tip used for comparative studies. Core diameter increases from 150 to 300 μm over 5 mm. Scale in millimeters. 39

FIGURE 4.4: (a) Diagram of pulse trigger structures by function generator. (b) Measured output temporal pulse profile of 50% duty cycle 500 μs pulse packet. 43

FIGURE 4.5: Detachable fiber tip design with twist locking mechanism. The trunk fiber contains the locking mechanism while the distal tip is simply outfitted with a keyed sleeve. (Top) Overall interface and detachable tip. (Bottom) Magnified twist locking region with transparent tubing to see internal geometry. 44

FIGURE 4.6: Photograph of detachable fiber tip twist-locking mechanism or “J-groove” with outer cover removed. 46

FIGURE 4.7: Laser lithotripsy setup consists of a human COM urinary stone submerged in a saline bath with the detachable fiber tip or the tapered fiber tip held manually in contact with the stone surface during laser irradiation. 48

FIGURE 4.8: (Top) Photograph of detachable fiber tip prototype with thermal images in air operating at 30 mJ pulse energy. Horizontal image width 100 mm. (Bottom) Tapered fiber tip with thermal images in air, image width 25 mm. 51

FIGURE 4.9: Spatial beam profiles for detachable and tapered fiber tips. (Top row) Magnified 300 μm core diameter distal fiber tips. (Bottom row) 50 mm away from distal fiber tip with box size 12.4 x 12.4 mm. 52

FIGURE 4.10: Distal fiber tip degradation as a function of pulse profile and total number of pulses. All fiber tips were held manually in contact with the stone during laser irradiation with 30 mJ pulse energy. Considerable fiber tip degradation was observed using the 20 Hz (Packet) for both fibers. 54

FIGURE 4.11: Distal fiber tip roughness measurement using a scanning white light interferometer. (a) Polished and before lasing. (b) After 60,000 500-μs pulses at a standard pulse rate of 50 Hz with a pulse energy of 30 mJ. Surface roughness measurements are from 50 x 50 μm cropped area, away from burns or pot marks. 55

FIGURE 5.1: Representation of suction effect on stone phantom. 63

FIGURE 5.2: Photograph of ~ 350 μm OD, 10 mm long stainless steel tube glued to 150 μm core diameter trunk fiber. 64

FIGURE 5.3: Scale representation of five fiber tips tested based on fiber recession distance. Length of stainless steel tube: 10 mm. 65

FIGURE 5.4: Petri dish (empty) with hollow fiber tip and side illumination. 65

FIGURE 5.5: Microscopic images of the hollow fiber tips compared to the bare fiber after 10 minutes at 150 Hz (90,000 total pulses). Decreasing tip degradation can be seen as fiber recession distance is increased. 68

FIGURE 5.6: Hollow fiber tip with fiber recessed (a) 100 and (b) 1000 μm operating at 150 Hz. Velocity was observed to increase along the optical axis with deeper fiber recession, and with increasing pulse rate. 69

FIGURE 5.7: Simultaneous Ho:YAG lithotripsy using a 200 μm core diameter fiber of a calculus can occur while the calculus is entrapped within the Escape^{TM} nitinol stone retrieval basket. Courtesy of Boston Scientific, Natick, MA [55]. 71

FIGURE 5.8: (a) Fiber muzzle attached to a 150 μm core diameter optical fiber, to control cavitation bubble expansion or retropulsion. Fiber is recessed 750 μm from distal end. Through hole diameter of ~ 350 μm and outer diameter of 643 μm. (b) Magnified image. 73

FIGURE 5.9: Fiber muzzle submerged in a water bath with suspended microspheres. Perpendicular water flow can be seen exiting the holes in the muzzle. (a) Muzzle through hole oriented horizontal. (b) Vertical. 74

LIST OF ABBREVIATIONS

a	radius
α	absorption coefficient
~	approximately
$\approx$	approximately equal to
au	arbitrary units
B_i	incident magnetic field
CaFl	calcium fluoride
CCD	charge-coupled device
COM	calcium oxalate monohydrate
dB	decibel
°C	degrees Celsius
Δ	change
dia	diameter
E_i	incident electric field
Er	Erbium
ex vivo	Latin: (out of the living)
FC	fiber connector
FLIR	forward-looking infrared
fps	frames per second
Fr	French (1 mm = 3 Fr)
FWHM	full width-half maximum
g	gram

GeO_2	germanium oxide
GRIN	graded-index
HCl	Hydrochloric acid
Ho	Holmium
HWG	hollow waveguide
in vivo	Latin: (within the living)
ID	inner diameter
IR	infrared
J	joule
KTP	Potassium titanyl phosphate
λ	wavelength
μ-	micro- (10^{-6})
m	meter
m-	milli- (10^{-3})
min	minute
N	number
n	index of refraction
n-	nano- (10^{-9})
NA	numerical aperture
NIDDK	National Institute of Diabetes and Digestive and Kidney Diseases
OD	outer diameter
OH	hydroxide
OPD	optical penetration depth

PDR	proliferative diabetic retinopathy
PFM	periodically-focused mode
Ra	profile roughness average
rms	root-mean-squared
Roc	radius of curvature
Rpv	profile peak-valley
Rq	profile roughness rms
s *or* sec	second
Sa	surface roughness average
SD	standard deviation
SMA	subminiature version A
Spv	Surface peak-valley
Sq	surface roughness rms
SWLI	scanning white light interferometer
θ_i	incident angle
θ_r	refracted angle
3D	three dimensional
TFL	Thulium fiber laser
UV	ultraviolet
W	watt
YAG	yttrium aluminum garnet

CHAPTER 1: INTRODUCTION

Over the past few decades, optical methods have become increasingly used to diagnosis diseases and provide therapeutic treatment. With the invention of the laser in the 1960s, many new treatment options for various diseases and cosmetics soon followed. A laser is unique in that it can provide highly directed light with small spectral bandwidth which has very specific tissue interaction properties. Depending on the energy and pulse duration of the laser light, tissue can be heated, coagulated, or vaporized. One property of using laser energy over conventional mechanical tools for surgery is the inherent hemostasis caused by thermal diffusion. Many types of medical lasers exist, however, new and improved lasers and alternative delivery methods are still invented every year.

Laser energy can be coupled into a fiber optic cable which can then be inserted into a natural orifice or surgical incision and delivered almost anywhere within the body. These endoscopic and laparoscopic approaches are currently used in such fields as urology, oncology and ophthalmology to coagulate, cut or ablate tissue. A typical optical fiber's distal ends are cleaved and polished for axial delivery of the laser radiation. However, various tip shapes have been used to create side-firing, diffusing or even focusing characteristics. These specialty tips can provide increased precision and performance for their intended treatment areas. The growing desire for less invasive medical treatment options and the rapid advancement in laser technology has generated a need for novel therapeutic approaches and fiber optic devices.

CHAPTER 2: OPHTHALMIC MICROSPHERE LASER SCALPEL

2.1: Background and Overview

2.1.1: Current Ophthalmic Surgical Techniques

As of 2004, 4.1 million people in the United States suffered from some form of diabetic retinopathy, and that number has steadily increased each year [1]. Preventative surgeries must be performed on these patients regularly to seal the leaking blood vessels on the retina. For this task, a KTP laser (λ = 532 nm) and multimode optical fibers are used to create hundreds of therapeutic lesions by photocoagulation alongside a vitrectomy procedure to remove debris in the eye [2]. In advanced cases, like proliferative diabetic retinopathy (PDR), the debris inside the eye settles forming encrusted layers as well as exudate deposits on the retina. As the density of these deposits increase, especially if they form on the macular region, vision becomes greatly impaired. The current surgical procedure for PDR requires the tedious use of micro-hook needles, forceps, and other instruments to remove deposits from the retina [3]. Incomplete removal of these deposits is the primary reason for retinal re-detachment and surgical failure rates. These tedious techniques create prolonged stress on the surgeon’s steadiness and the patient’s eye allowing for errors like accidental puncture, tearing and detachment. For these reasons, the surgical procedure for PDR, advanced retinopathy of prematurity, and other similar intraocular surgeries could benefit from an ultra-precise contact laser probe for ablation of ophthalmic tissues. Conventional fiber optic based surgical laser probes are designed to operate either at a fixed working distance from the tissue or in contact with the tissue with relatively large spot diameters (e.g. > 100 μm). These fibers and laser probes are not widely used in intraocular laser surgery, except for thermal coagulation, because they lose their ability to focus light in aqueous media. In contrast, the novel laser probe discussed below may operate to ablate the tissue in contact mode.

The highly diverging and small spatial beam size at the probe's surface combined with the short optical penetration depth of the Er:YAG laser may allow better surgical results in more sensitive and thin areas like the macula where detailed vision is achieved and surgical precision is most important. Replacement of mechanical intraocular surgical instruments with a laser probe that has a much smoother tip with a tractionless method for tissue engagement may also reduce mechanical retinal surface damage as well as retinal detachments [4].

2.1.2: Erbium:YAG Laser for Tissue Ablation

The Erbium:YAG laser is currently used in the medical fields of dermatology [5, 6], dentistry [7, 8], and ophthalmology [9-15] because the 2940 nm wavelength closely matches a major water absorption peak in tissue (Figure 2.1), resulting in an optical penetration depth (OPD) of approximately 5-10 μm for soft tissues. The ablation threshold needed to achieve soft tissue removal using the Er:YAG laser is ~ 0.016 J/mm^2 [16] and thermal damage depths at the bottom of the ablation craters created in cornea tissue at high fluence are between 10-50 μm [17]. In the case of PDR surgery, the Er:YAG laser's short OPD will mean ablating the exudate deposits while minimizing thermal damage to the underlying retina, which is critical. Since most current applications of the Er:YAG laser are in dermatology and dentistry, where the tissue is readily accessible, a waveguide or fiber, although preferred, is not required to deliver the laser energy to the tissue. However, for endoscopic applications, like intraocular surgery, a specialized fiber optic delivery system is required because common silica based fibers do not transmit beyond ~ 2500 nm. Germanium oxide mid-IR fibers and hollow waveguides have been developed and tested to overcome this issue, and they provide flexibility and high transmission. Previous studies have been reported using the Er:YAG laser during vitrectomy procedures by D'Amico, Joseph and Hoerauf [12, 18-23]. These studies did not use contact probes but fibers and devices at varying distances from retinal and membrane tissue with spot sizes greater than 100 μm.

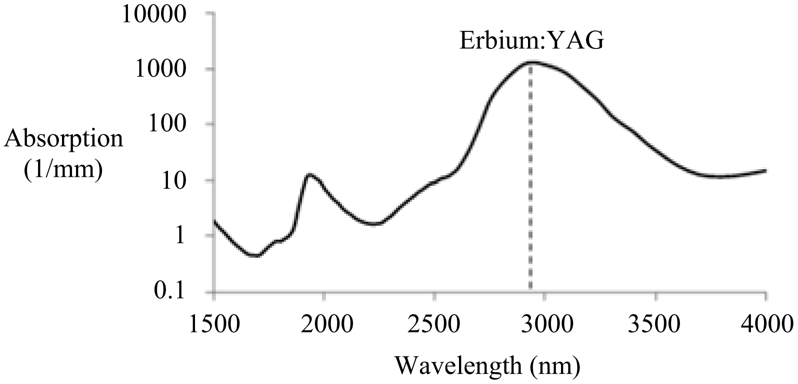

Figure 2.1: Water absorption data plotted across mid-IR wavelengths. Peak absorption occurs at λ=2940 nm [24].

2.1.3: Surgical Laser Microprobes and Microspheres

Over the past twenty years various optical devices including spheres [25], hemispheres, domes, cones, slanted shapes [26, 27], cylindrical gradient index (GRIN) lenses [28], and tapered fibers have been used as tips for ophthalmic laser scalpels.

However, these devices are typically designed to operate in non-contact mode in air at a fixed working distance from the tissue. Contact mode probes can be created by placing a single sphere with a high index of refraction, between 1.7 and 2.0, at the end of a waveguide or optical fiber. Spheres at these indices will focus an incident plane wave on the back surface to a focal point near the front surface. Fast focusing through the sphere also creates a fast divergence after the sphere. This property can be used to decrease the effective penetration depth in tissue by allowing only the light near the surface of the sphere to have an energy density sufficient to ablate tissue. Working in contact mode minimizes any intervening water layer which would otherwise strongly attenuate the mid-IR laser radiation.

Recently, chains of microspheres in odd multiples at these indices have been shown to reduce the spot size of the laser beam through filtering of non-periodically focused modes (PFM) [29, 30]. Even numbered spheres re-collimate while odd numbered spheres refocus. Sphere chains are known to reduce transmission as the chain length increases due to Fresnel losses and mode filtering. However, by reducing the beam size our applications also require lower laser pulse energy requirements than other fiber delivery probe devices. Furthermore, the transmission loss of a spherical lens is significantly less than a pinhole with a diameter equal to a sphere's beam waist. The purpose of this study is to test a mid-IR laser and novel fiber optic probe for precise ablation of a thin layer of tissue, in contact mode, with minimal collateral thermal damage to underlying tissue, for potential application in ophthalmic surgeries.

2.2: Design and Testing of Microsphere Scalpel

2.2.1: Laser Source and Fiber Delivery

An Erbium:YAG laser (Model 1-2-3, Schwartz Electro-Optics, Orlando, FL) operating at a wavelength of 2940 nm, in normal-spiking mode with a pulse duration of 75 µs (Figure 2.2), and pulse repetition rate of 5 Hz was used in these studies. Pulse energies of 0.02 – 1.0 mJ were used. A 2-m-long, 150-µm-core-diameter germanium oxide mid-IR optical fiber (Infrared Fiber Systems, Silver Spring, MD) was used to guide the laser energy to the scalpel. The fiber core has a refractive index of 1.84 with an attenuation of 0.7 dB/m at a wavelength of 2940 nm.

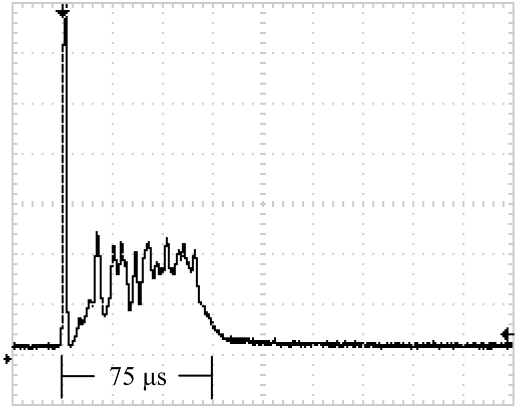

Figure 2.2: Er:YAG normal-spiking mode 75 µs pulse profile.

2.2.2: Microsphere Scalpel Design

During preliminary studies, three types of spheres were tested to determine their candidacy for use in the surgical probe: sapphire, borosilicate, and barium titanate. The silica glass spheres ($n \approx 1.47$ at $\lambda = 2940$ nm) did not focus close to the surface of the sphere due to the low refractive index, and therefore also failed to provide surface focusing in longer chains. Barium titanate (*n*≈1.9 at λ=2940 nm) provided good surface focusing and spot size reduction in longer chains, but suffered from very low transmission at λ = 2940 nm and also had a low damage threshold of ~ 3 mJ. For our experiments we chose to use sapphire spheres with diameters of 300 µm and 350 µm (Swiss Jewel Company, Philadelphia, PA). Sapphire provides low attenuation and has a refractive index of 1.71 at λ = 2940 nm, to provide focusing near the front surface. Geometrical ray trace simulations have shown that chains of spheres with a refractive index close to 1.7 provide the smallest spatial beam width at the surface of the end sphere [31]. Sapphire is also biocompatible, has a high phase transition temperature, and a high laser damage threshold. The spheres used had tight diameter tolerances and a low number of inclusions. No damage to the sapphire spheres was noticed at pulse energies up to 10 mJ.

The structure of the scalpel was a semi-rigid and robust silver lined 300 µm inner diameter, 750 µm outer diameter, silica hollow waveguide (HWG) (HWCA300750**,** Polymicro Technologies, Phoenix, AR). Current mechanical instruments used in ophthalmic surgery have overall diameters of approximately 1 mm, so our design can be easily integrated into existing surgical techniques. In these studies we used 30 mm HWGs in a straight configuration with a maximum loss of 2.0 dB/m at λ = 2940 nm. Since the HWG is the support structure of our probe, a length of 30 mm was determined to be the minimum length that would be necessary to reach the retina from outside the eye (Figure 2.3). To be a multipurpose ophthalmic scalpel used for surgeries throughout the eye, all corneal and retinal testing as well as ray trace modeling was performed under this required design constraint.

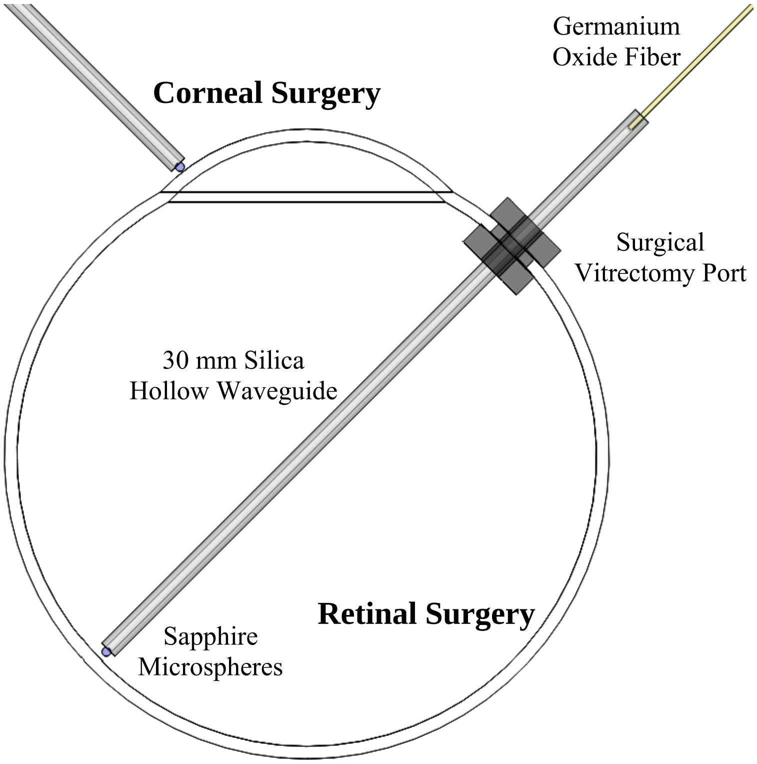

Figure 2.3: Proposed ophthalmologic surgical configurations consisting of a 30-mm-long hollow waveguide of 0.75-mm-diameter with microsphere focusing at distal tip. The diameter of a typical human eye is 24 mm [32].

2.2.3: Microsphere Scalpel Construction

These waveguides provide an optical conduit, allowing insertion of the germanium oxide fiber on the proximal end and gluing of a sphere or sphere chain on the distal end. The end of the scalpel must be sealed to prevent liquid leaking into the waveguide and altering the focusing properties of the sphere chain. This was achieved by placing a slightly larger diameter end sphere of 350 μm, compared to the inner diameter of the HWG (300 μm), on the tip of the HWG and then gluing it in place with UV cured epoxy (Norland Optical Adhesive #61, Cranbury, NJ) using micromanipulation and a small wire. Appendix A further details the gluing of the microsphere onto the hollow waveguide. Additional 300 μm spheres were then inserted into the proximal end and pushed into contact with the glued sphere to create multiple sphere structures. Our experimental setup was in a vertical orientation so the spheres inside the HWG remained in contact. Future work will be necessary to provide a more robust and permanent method of fixing the internal spheres without compromising the optical path.

2.2.4: Experimental Tissue Setup

Fresh porcine eyes were harvested and used immediately after sacrifice of pigs from unrelated experiments. The cornea was chosen in this preliminary study as a simple model for ophthalmic tissue ablation experiments for several reasons, including its ease of use concerning dissection, preservation, processing, and analysis after laser tissue ablation. Preliminary test results performed on retinal tissue are not shown because our current capabilities hinder us from recording measurements on retinal craters. This was due to the fact that the microscopic ablation craters were difficult to distinguish visibly, and our histological fixation methods induced a large amount of stress on the fragile retina therefore destroying the samples.

The Er:YAG laser beam was coupled directly into a 2-m-long, 150-μm-core germanium oxide fiber. The fiber's distal end was then inserted 1 mm into the proximal end of the vertically positioned 30-mm-long HWG with the glued 350 μm sphere on the bottom. Tissue ablation experiments were then performed by bringing the cornea tissue into gentle contact with the various probe configurations and translating the sample, *ex vivo*. The cornea was kept hydrated prior to each test by applying a single drop of Tetrahydrozoline HCl 0.05%, common over the counter eye drop solution. The relatively low laser pulse rate of 5 Hz allowed creation of hundreds of single pulse craters along this path over a period of 60 s.

2.3: Results

2.3.1: Microsphere Scalpel Characterization

Characterization of the probe's beam shaping performance was conducted before tissue studies. One, three, and five sphere structures were tested to determine their relationship to spot size and transmission. The top rows of Figures 2.4 and 2.5 show the simulation results for intensity distribution at the minimum spot size after the end sphere, approximately 10 µm from the vertex. The full width half maximum (FWHM) measured from the simulation for each configuration of one, three, and five spheres is 8, 9, and 4 µm, respectively. For comparison, this was measured experimentally using a 12.7 mm focal length calcium fluoride lens to magnify and image the minimum waist size near the sphere's surface. An infrared beam profiler (Pyrocam III, Spiricon, Logan, UT) was positioned 500 mm from the magnification lens. To calibrate the magnification an empty HWG was used to reference 300 µm. Since the output of the multimode fiber has an unpredictable mode orientation depending on its length, bends and coupling, the images captured by the beam profiler were averaged while gently flexing the fiber near its mid-length point. This motion generated random mode orientation patterns hitting the sphere chains, thus creating repeatable profile measurements. The averaged beam profiles for the tested structures are shown in Figure 2.4. The FWHM measured for each configuration of one, three, and five spheres is 67, 32, and 30 µm, respectively. An increasing lower intensity ring spreading away from the central peak for increasing number of spheres in the chains can be seen.

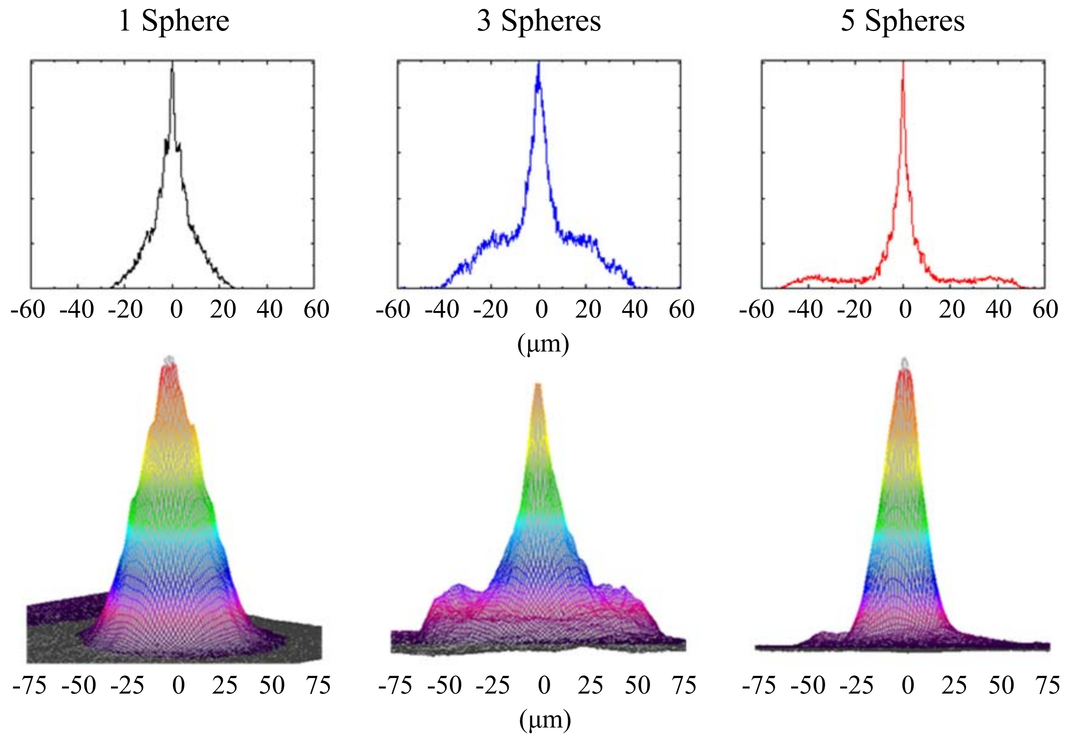

Figure 2.4: (top row) Normalized simulation of the intensity measured at the minimum beam waist (FWHM) for one, three, and five sphere configurations. Courtesy of Arash Darafsheh. (bottom row) 3D beam profiles acquired by magnifying the minimum beam waist onto the IR beam profiler's detector array. As the number of spheres increase a reduction in (FWHM) spot diameter and an expanding low intensity mode filtering ring can be seen in both simulation and experiment.

2.3.2: Ablation Crater Measurements on Corneal Tissue

Various pulse energies between 0.02 - 1.0 mJ at a duration of 75 μs were tested to experimentally determine the ablation threshold of the cornea. With an average beam diameter of ~ 50 μm, craters began to form at a pulse energy of 0.1 mJ corresponding to an energy density of ~ 0.05 J/mm^2. Single pulse craters were formed on hydrated cornea tissue using this near threshold pulse energy of 0.1 mJ. Pulse energy was measured using a pyroelectic detector (ED-100A, Gentec, Saint-Foy, Canada) near the tip of the probe. Single, three, and five sphere structures were tested and the tissue was imaged and measured with a FS70 Mitutoyo microscope equipped with a CCD camera (Edmund

Optics, Barrington, NJ). Since each sphere chain configuration (1, 3, or 5 spheres) attenuated the energy differently, attenuation of the laser output was adjusted to normalize each configuration to an incident energy of 0.1 mJ on the tissue surface. Over 50 craters for each structure were measured and the average crater widths are shown in Table 2.1 along with representative images for each in Figure 2.5.

Table 2.1: Corneal ablation crater dimensions at pulse energies of 0.1mJ (S.D. = 10 µm).

	1 sphere	3 spheres	5 spheres	Trend
Crater Width	44 µm	30 µm	17 µm	Decreases
Crater Depth	26 µm	10 µm	8 µm	Decreases
Lateral Thermal Damage	29 µm	33 µm	39 µm	Increases
Depth of Thermal Damage	< 5 µm	33 µm	22 µm	Varies

Histologic analysis was performed on the corneas to quantify ablation crater and thermal damage depths. The crater diameters were measured using light microscopy immediately after the procedure, and then the eyes were placed in formalin. Eyes were sectioned and the extra material was discarded leaving only the polar cornea region. The corneas were trimmed for histological processing and various samples were stained with either trichrome or hematoxylin-eosin. The craters were viewed and measured using the Mitutoyo microscope. Over 10 trichrome stained histology craters for each structure were measured and the average crater depths are shown in Table 2.1 along with representative images for each shown in Figure 2.5.

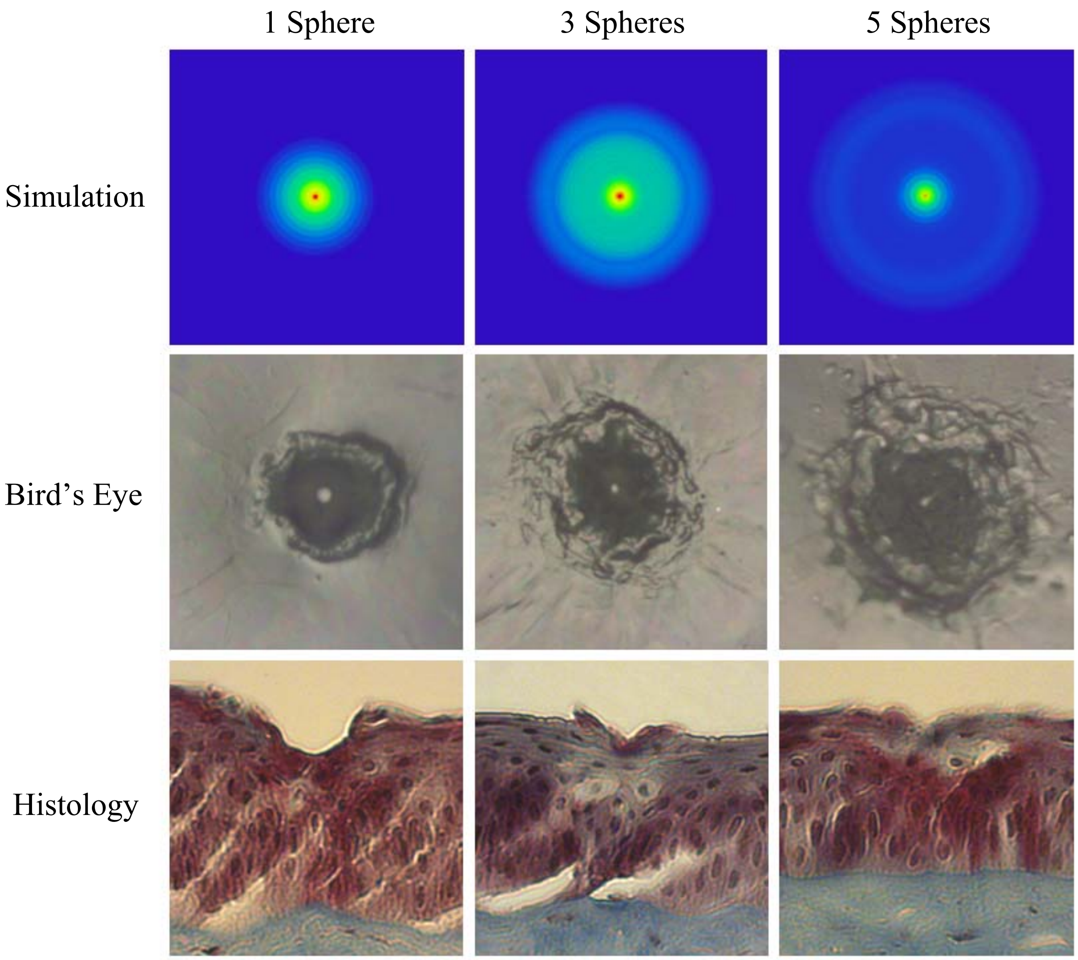

Figure 2.5: Simulated intensity profiles for one, three, and five sphere probes at minimum spot size occurring at 10 μm after sphere vertex, courtesy of Arash Darafsheh (Top row). Representative bird's eye corneal crater images for one, three, and five sphere probes at 0.1 mJ (Middle row). Representative histology images for one, three, and five sphere probe craters at 0.1 mJ with trichrome stain (Bottom row). Each cell size: 120 x 120 μm.

2.4: Discussion

Short ablation depths with small thermal damage regions have been achieved with Er:YAG laser probes in previous studies [12, 17-23]. However, our contact mode mid-IR microsphere scalpel can create spatially small ablation craters below the limit of current intraocular fiber delivery systems, while using a less powerful laser source. Sapphire microspheres with a refractive index of 1.71 at λ=2940 nm, used as lenses, focus laser light at the sphere's surface creating a robust contact laser device where the transmission medium will not affect the device's performance. By building these sphere chains inside an air filled hollow waveguide's tip and sealing it to the end sphere, all internal focusing surfaces maintain their relative refractive indices even when submerged in the vitreous.

2.4.1: Uncertainty in Characterization Results

The overall energy output decreases with increasing number of spheres due to non-PFM filtering. This can be seen by examining the output beam profiles of each sphere structure. However, the FWHM spot diameter decreases and the peak energy only slightly decreases. Fresnel equations predict an ~ 25% decrease for every odd numbered sphere or four sapphire/air interfaces, which is confirmed in our testing. The low intensity region around the central peak, seen in the three and five sphere chain, is believed to be due to the mode filtering. It is important to realize that the simulations represent an ideal case of perfectly aligned spheres and fiber output on one axis as well as defect free materials. Geometrical modeling of sphere lenses shows that they can produce a NA = 1 or sometimes larger for chains, and therefore all the rays cannot be captured by our imaging system (Figure 2.6). This means that the FWHM measurements stated earlier only show what is occurring in the on-axis cone NA = 0.5 which corresponds to our magnification lens. This could also explain why the low intensity region in the five sphere beam profile is not visible in Figure 2.4 but is contributing in Figure 2.5 to tissue thermal damage because the rays were so off-axis they were not captured by the imaging system. Future work will be conducted to fully capture and characterize the beam exiting the sphere structures. The slight lean of each peak can be explained by the spheres inside the HWG not being perfectly aligned on-axis and the fiber tip not perfectly centered and aligned in the input end of the HWG.

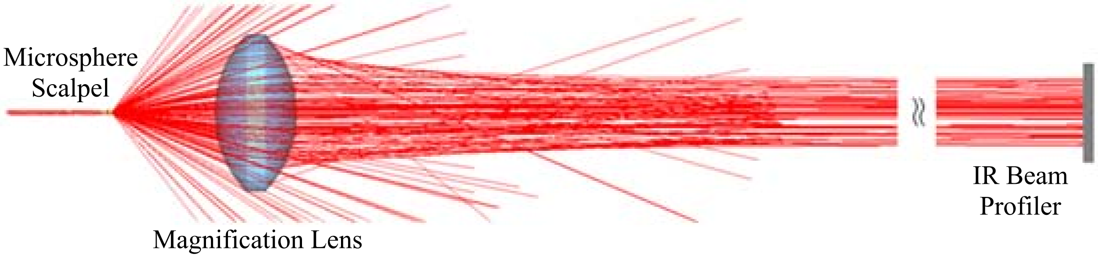

Figure 2.6: Beam characterization of the microsphere probe using a NA=0.5 magnification lens to focus the minimum waist onto the infrared beam profiler's detector array 500 mm away. Rays beyond the numerical aperture of the lens were not characterized experimentally but are present in simulations and tissue testing since the device operates in contact mode with tissue. The simulation was performed using FRED.

2.4.2: Tissue Results

The ablation crater widths in corneal tissue decreased on average with increasing chain lengths, comparable to the characterization. However, by visual inspection the lateral thermal damage regions increased (Figure 2.5). One cause for this larger thermal region may be the filtered non-PFMs which create a low intensity region. The lower intensity region visible in the three sphere beam profile (Figure 2.4) is below the ablation threshold but is still sufficient to create thermal damage. The numerical aperture or angle of the rays exiting the end sphere also increases with increasing sphere chains, spreading the energy over a larger area and decreasing the energy density once the rays leave the scalpel and enter the tissue. These filtered modes and increasing angles cause the five sphere chain to produce even greater thermal damage as seen in Figure 2.5.

Ablation crater depths on corneal tissue were measured between 10 - 25 μm (Table 2.1 and Figure 2.5). While retinal tissue has different optical and mechanical properties than cornea, by using the Er:YAG laser which has such a strong water absorption peak, future retinal tissue ablation results may be comparable. Removal of small deposits with thicknesses between 20 - 50 μm on top of the retina, while minimizing damage to the retina which has a thickness ranging between 150 - 300 μm, is the primary goal of this scalpel design. Average ablation crater depth for each structure decreased with an increase in sphere chain length. However, the thermal damage zones increased for multiple sphere chains. The numerical aperture of the rays entering the tissue may be responsible for this result because the gradual spreading of these rays increases the lateral thermal damage. This could also explain the increase in thermal depth for three spheres and then the decrease in depth for five spheres. The three spheres did not have sufficient perpendicular directionality to ablate deeper than one sphere, but still had steeper angles than the five sphere structures to direct the thermal depths deeper. Instead, the five sphere chain which had the highest numerical aperture directed the energy more laterally from the sphere tip. In the single sphere case the beam is more normal and therefore directs the energy deeper, ablating more tissue with less, if any, noticeable thermal damage. These average thermal damage trends were noticed in almost all histology craters examined. Multiple sphere chains result in a more diverging beam at the sphere tip and spread the same, normalized, energy over a larger volume after entering the tissue, decreasing ablation and increasing thermal damage. In all samples measured, including other studies with higher pulse energies greater than 0.2 mJ, three and five sphere structures consistently produced more thermal damage. Simulations with tissue scattering/absorption modeling should be performed to better explain these findings.

2.4.3: Possible Improvements

Several improvements can be made to the probe design. Modeling has shown that the spot size will decrease if the sphere diameters are reduced, and if all the spheres are the same diameter, including the end sphere [31]. We chose a slightly larger end sphere for this study for its ease of assembly, but it should be possible to fix and seal a smaller sphere at the HWG tip with more precise methods. Also for a practical device the internal spheres will have to be fixed in some way. Work is also being conducted to further reduce the spot size by improving the input beam profile. Single mode germanium oxide fibers or other waveguides optimized for 2940 nm are not currently available, as these would be ideal for delivering the smallest spot sizes and improved spatial beam profiles. Preliminary testing has demonstrated a factor of six size reduction compared to FWHM diameters reported in Figure 2.4 for same structures with near single mode input beams. However, to accomplish this task for a practical application the laser output must be directly applied to the sphere structures.

Although not observed or characterized in this preliminary study with corneal tissues, it is possible that exploding and imploding vapor bubbles at the treatment site may result in mechanical damage to other more delicate ophthalmic tissues of interest such as the retina, which do not have the same robust mechanical properties as the cornea. We believe that these bubbles are highly localized and shallow, and therefore will not cause significant mechanical tissue damage due to the low pulse energy, small spot diameter, and contact mode application of our probe. However, further detailed studies utilizing a high-speed camera to directly image the cavitation bubble dynamics during mid-IR ablation of both corneal and retinal tissues will be necessary in future work to confirm these claims. Regardless, water is still the primary absorber at the mid-IR wavelength of 2.94 μm for both tissues, so the optical properties of the tissues should be more similar than the mechanical properties. Finally, this probe design should be easily translatable from an air environment described in these preliminary studies with the corneal samples to a fluid environment utilizing retinal tissue for potential PDR applications since the device works in contact mode and is water-tight.

2.5: Conclusions

A 750 µm outer diameter intraocular scalpel utilizing microsphere lenses was developed capable of delivering Er:YAG laser pulse energy to ocular tissue, and creating ablation craters with widths between 15 - 50 µm in contact mode. Different scalpel configurations with varying sphere chain lengths were successfully tested under *ex vivo* conditions on corneal tissue near the ablation threshold, demonstrating ablation crater size reduction for increasing number of microspheres, but with an increase in thermal damage. The small spatial beam size combined with the short optical penetration depth of less than 20 µm could make this probe useful for precise contact ablation of exudates during surgery for proliferative diabetic retinopathy. Future studies will involve further development of the microsphere probe and *in vivo* studies in a PDR animal model.

CHAPTER 3: OPTIMIZATION & PACKAGING OF MICROSPHERE SCALPEL

3.1: Previous *ex vivo* Study

In the previous chapter, an optical scalpel was tested using *ex vivo* porcine corneas as a simple, robust ophthalmic tissue model. The ablation threshold for *ex vivo* porcine cornea samples was found to be ~ 0.013 J/mm^2 (pulse energy ~ 25 μJ, FWHM spot diameter ~ 50 μm). This ablation threshold corresponds well with that reported in previously published studies, 0.001 – 0.010 J/mm^2 using the Er:YAG laser for ablation of various soft tissues.

Although these results showed the potential advantages of using such a device in intraocular laser surgery, the design of the focusing structure was sub-optimal in previous studies. The focusing was provided slightly in front of the end-sphere which, in principal, should lead to deeper ablation craters which is undesirable for dissecting and laminating of the fibrotic membranes with controllable and shallow depth. The sub-optimal feature of this previous design was due to the observation that all scalpels tested contained a larger diameter glued distal sphere (350 μm) followed by smaller diameter spheres inside the waveguide to generate the odd-numbered focusing chains. The reason for selecting this structure was due to difficulties of fabrication of optimal structures formed by uniform size spheres.

This chapter shows the assembly and testing of optimal structures formed by chains of identical sapphire or ruby spheres with n=1.71 at λ=2940 nm. Numerical modeling also shows that the optimal structures focus light exactly at the tip of the end sphere which leads to an important advantage of these structures for achieving shallow and controllable depth of surgery. The cavitation bubble inevitably occurs in such surgeries near the tip of the device. However, in the optimally designed structures the beam is extremely divergent inside such bubbles and should significantly slow down the rate of tissue ablation once the depth of the bubble reaches ~10 µm. This mechanism can be considered as a built-in safety feature for reducing the retina damage during dissection of unhealthy fibrotic membranes or other ultra-precise surgical procedures. Additional tissue studies were performed with the new structures at higher pulse energies to demonstrate the rapid decrease in ablation depth. Finally, the microsphere scalpel is integrated with other surgical instruments into a single handpiece.

3.2: Materials and Methods

3.2.1: Theoretical Modeling

Theoretical modeling was performed with Zemax (Radiant Zemax LLC, Redmond, WA), a commercial optical design software package. The main components are the laser light source, laser delivery system, and focusing elements. As illustrated in Figure 3.1, it is assumed that a multimode fiber (e.g. germanium oxide fiber) with a core diameter of $2a$=150 µm and with NA=0.12 is inserted into a HWG (a hollow glass waveguide) with an internal diameter of $2a$=300 µm. These dimensions are typical for mid-IR waveguides [33]. Smaller HWG diameters would allow more compact focusing of the beams, however diameters smaller than $2a$=300 µm are rarely used in practice because of the strongly increasing propagation losses $\alpha \sim 1/a^3$, where α is the attenuation coefficient [33]. The end-sphere was placed close to the HWG edge in a configuration where half of the end sphere was extended from the HWG as depicted in Figure 3.1 for a 5-sphere chain. In our previous studies, this structure was optimized for the best performance in contact with tissue [31].

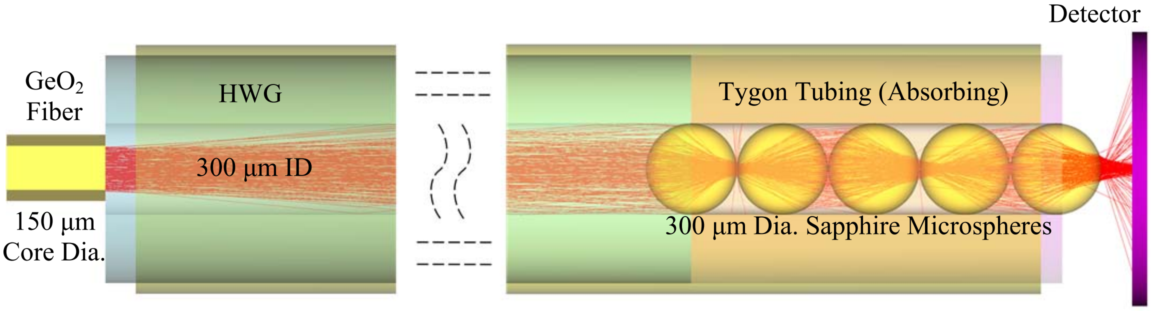

Figure 3.1: A focusing microprobe design based on arrays of spheres placed in a hollow waveguide. Courtesy of Arash Darafsheh.

To model the device operation in the presence of cavitation bubbles, we placed the detector at different distances from the tip of the device in the medium with *n*=1 and calculated the beam profile at different distances from the tip, as illustrated in Figure 3.2a-c for *N*=1, 3, and 5 sphere chains, respectively. In a real surgical environment, the vaporized tissue would create a bubble just at the tip of the sphere, and the light would propagate through this bubble. In our modeling we neglected the light absorption inside the bubble and assumed that the vapor index is close to *n*=1. The irradiance profiles in Figure 3.2 effectively represent the irradiance distribution at the distant bubble sidewall. The red dashed lines are used as a guide to represent how the irradiance peak of the beam reaching the opposite sidewall of the bubble depends on the bubble diameter. It is seen that for a single sphere and 3-sphere chain the irradiance peak experiences slow variations as the bubble grows. The irradiance peak for 5-sphere chain shows a peculiar behavior which can be very useful for controlling the depth of surgery. Once the bubble reaches about 10 μm size the irradiance peak drops by a factor of four and stays at this low level for bubble sizes increasing up to 20-30 μm. This situation indicates the possibility that the depth of the ablation craters in tissue would saturate at the 10-20 μm level in practical surgery.

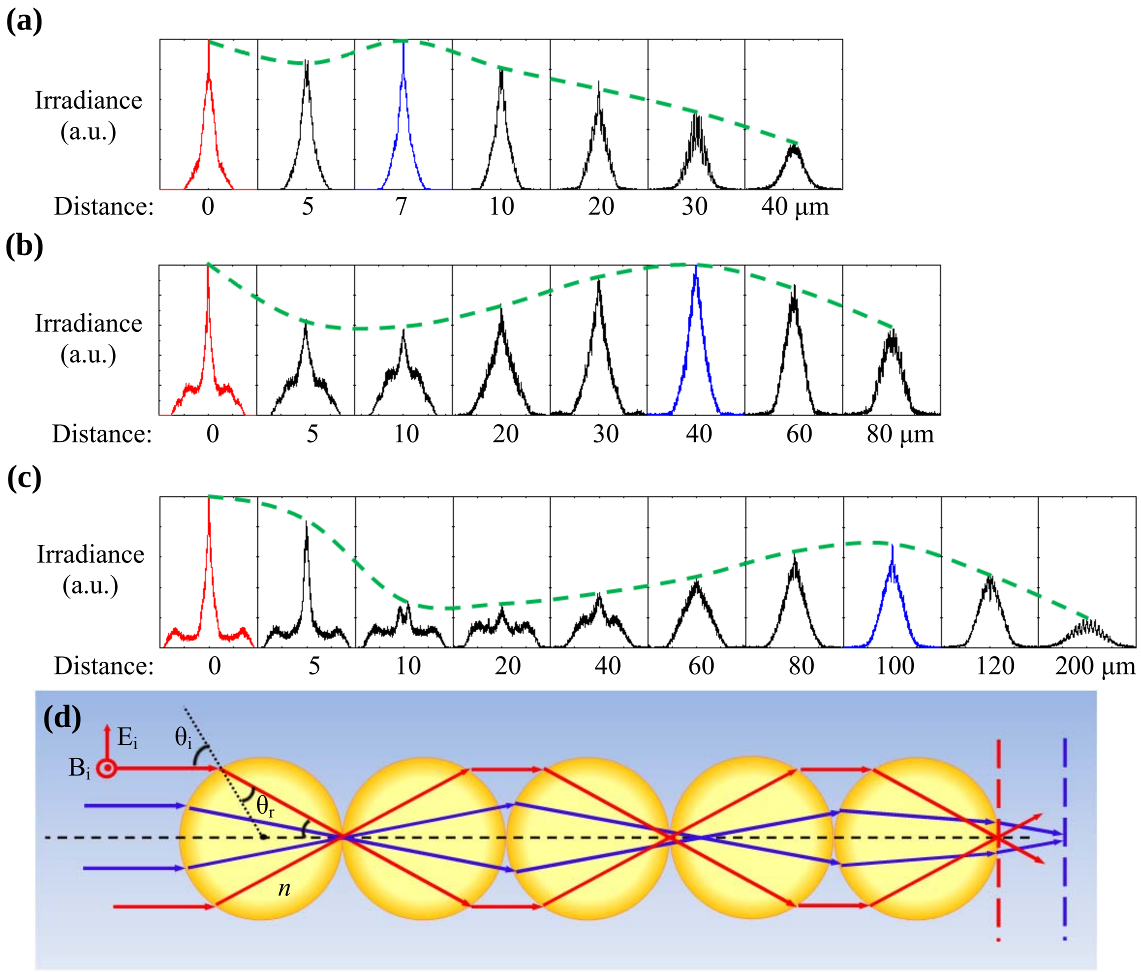

Figure 3.2: Irradiance distribution for different distances from the tip of a microprobe composed of (a) 1, (b) 3, and (c) 5 spheres with n=1.71. (d) Red rays correspond to PFMs which provide sharp focusing at the surface of every odd number of spheres. Blue rays correspond to paraxial rays. Courtesy of Arash Darafsheh.

3.2.2: Microsphere Scalpel Detachable Tip with Illumination

To create the microsphere scalpel with identical sphere diameters a flexible Tygon tube with an inner diameter of 250 μm was used to secure the 300 μm diameter sapphire spheres (Swiss Jewel Company, Philadelphia, PA), as shown in Figure 3.3 The tight-fitting Tygon tubing provided a waterproof seal at the distal tip. The sphere chain was then placed in front of the hollow waveguide with inner and outer diameters of 300 and 750 μm, respectively, and both were secured together inside a thin-wall polyimide tube (B000PHAI3M, Amazon Supply, Seattle, WA). A small ring of glue was then applied to secure the polyimide to the Tygon tubing.

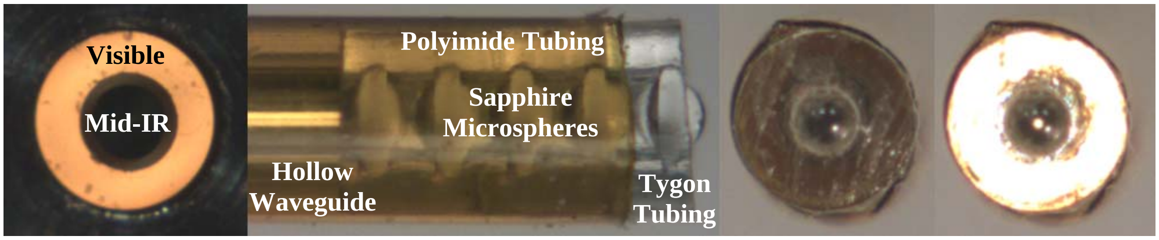

Hollow Waveguide (Proximal)

5 Microsphere Mid-IR Laser Scalpel (Distal)

Illumination (ON)

Illumination (OFF)

Figure 3.3: Detachable microsphere scalpel with integrated illumination.

Previous studies were performed with a probe created by inserting and fixing a flexible, 2-meter-long, 200-µm-OD germanium oxide fiber into the proximal end of the hollow waveguide. In this work, a simple self-aligning detachable tip was created by gluing the proximal end of the hollow waveguide inside a 770-µm-inner-diameter SMA connector (10770A, Thorlabs). The dual fiber connector and the hollow waveguide connector were then joined with a SMA mating sleeve (ADASMA, Thorlabs). Using a hollow waveguide with a length of 60 mm allowed for a probe needle length of about 35 mm, or roughly the length of current intraocular instruments.

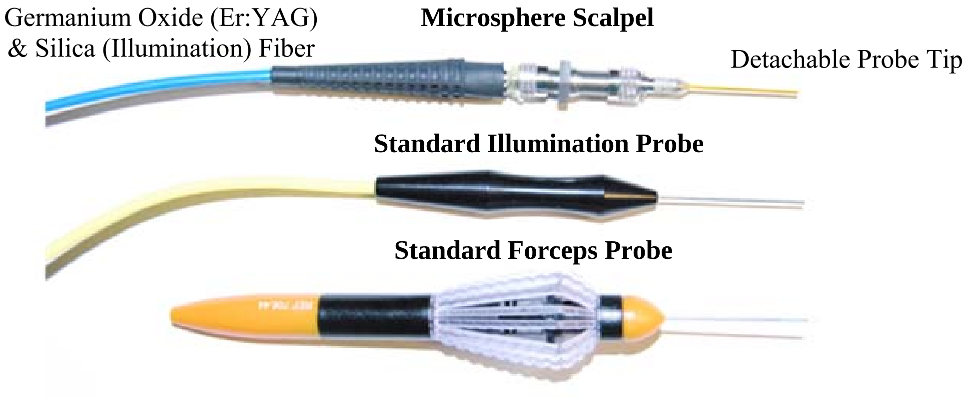

Figure 3.4: Detachable microsphere scalpel prototype compared to two common ocular surgical instruments, each of which are 23 gauge (~625 µm). For the microsphere scalpel, two standard SMA fiber connectors are integrated using a mating sleeve.

The illumination functionality (Figure 3.3) was achieved by using the buffer of the mid-IR HWG made from silica as a waveguide for visible light. A separate 200-µm-core-diameter silica fiber (AFS200/220Y, Thorlabs Inc, Newtown, NJ) coupled to a white light source was used to deliver illumination light to the silica cladding region of the hollow waveguide in the scalpel. This was achieved using a separate 230-µm-ID SMA fiber optic connector (10230A, Thorlabs) integrated with the connector to HWG shown in the top image in Figure 3.4 Both fibers were then encased in a Kevlar protective fiber jacket (FT030, Thorlabs).

3.2.3: Experimental Tissue Setup

The Er:YAG laser and the germanium oxide fiber used were identical to the studies in chapter 2, with the exception of the output pulse energy which was increased to ~ 200 µJ from ~ 100 µJ.

Fresh porcine eyes were harvested and used immediately after sacrifice of pigs at a local slaughterhouse from unrelated experiments. The cornea was chosen in this preliminary study as a simple model for ophthalmic tissue ablation experiments for several reasons, including its ease of use concerning dissection, preservation, processing, and analysis after laser tissue ablation. Preliminary test results performed on retinal tissue are not shown because our current capabilities hinder us from recording measurements on retinal craters. This was due to the fact that the microscopic ablation craters were difficult to distinguish visibly, and our histological fixation methods induced a large amount of stress on the fragile retina therefore destroying the samples.

Tissue ablation experiments were then performed by bringing the cornea tissue into gentle contact with the various probe configurations and translating the sample, *ex vivo*. The cornea was kept hydrated prior to each test by applying a single drop of Tetrahydrozoline HCl 0.05%, common over the counter eye drop solution. The relatively low laser pulse rate of 5 Hz allowed creation of hundreds of single pulse craters along this path over a period of 60 s.

3.3: Results and Disscussion

3.3.1: Tissue Study

Single pulse craters were formed on hydrated cornea tissue using a pulse energy of ~ 0.2 mJ, just above the ablation threshold of ~ 0.016 J/mm^2. Pulse energy was measured using a pyroelectic detector (ED-100A, Gentec, Saint-Foy, Canada) near the tip of the probe. Single, three, and five sphere structures of identical sphere size were tested and since each sphere chain configuration (1, 3, or 5 spheres) attenuated the energy differently, attenuation of the laser output was adjusted to normalize each configuration to incident energy of ~ 0.2 mJ on the tissue surface.

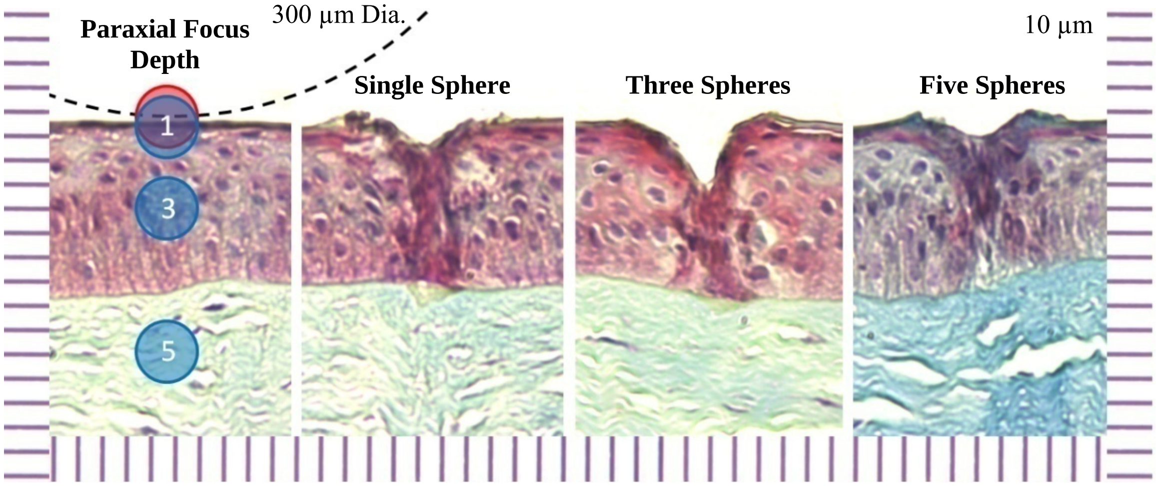

Figure 3.5: Trichrome histology of ablation craters created in epithelium layer of cornea using detachable microsphere scalpel with integrated illumination.

Histologic analysis was performed on the corneas to quantify ablation crater and thermal damage depths. Immediately after the procedure the eyes were placed in formalin. With the pupil center being the pole, the eyes were sectioned latitudinal and the extra material was discarded leaving only the polar cornea region. The corneas were trimmed to ~ 1 mm thick longitudinal sections for histological processing and various samples were stained with Masson's Trichrome. The craters were viewed and measured using a microscope equipped with a CCD camera. A representative image for each sphere configuration is shown in Figure 3.5 An additional native cornea histology image is shown to visualize the PFM and paraxial foci of the 300 μm diameter sphere configurations. Ablation craters depths of 12, 25, and 10 μm and thermal damage depths of 70, 40, and 30 μm were measured for one, three, and five spheres, respectively. The staining/coloring was inconsistent between batches. The darker colored region corresponds to thermal damage.

3.3.2: Discussion

Short ablation depths with small thermal damage regions were achieved with Er:YAG laser probes in previous studies [4, 9-23]. However, our contact mode mid-IR microsphere scalpel can create spatially small ablation craters below the limit of current intraocular fiber delivery systems, while using a less powerful laser source. Sapphire microspheres with a refractive index of 1.71, used as lenses, focus laser light at the sphere's surface creating a robust contact laser device where the transmission medium will not affect the device's performance. By building these sphere chains inside an air filled hollow waveguide's tip and sealing it to the end sphere, all internal focusing surfaces maintain their relative refractive indices even when submerged in the vitreous.

Ablation crater depths on corneal tissue were measured between 10 - 25 μm. Previous studies were performed with a less optimal larger end sphere and at a pulse energy of ~ 0.1 mJ. In contrast, this study used identical diameter spheres and a pulse energy of ~ 0.2 mJ. Much smaller depth of ablation craters and a more compact thermal damage zone observed for the 5-sphere chain can be related to the mechanism of self-limiting depth of surgery schematically illustrated in Figure 3.2c. While retinal tissue has different optical and mechanical properties than cornea, by using the Er:YAG laser which has such a strong water absorption peak, future retinal tissue ablation results may be comparable. Removal of small deposits with thicknesses between 20 - 50 μm on top of the retina, while minimizing damage to the retina which has a thickness ranging between 150 - 300 μm, is the primary goal of this scalpel design.

Although not observed or characterized in this preliminary study with corneal tissues, it is possible that exploding and imploding vapor bubbles at the treatment site may result in mechanical damage to other more delicate ophthalmic tissues of interest such as the retina, which do not have the same robust mechanical properties as the cornea. We believe that these bubbles are highly localized and shallow, and therefore will not cause significant mechanical tissue damage due to the low pulse energy, small spot diameter, and contact mode application of our probe. In our theoretical model we assumed that these cavitation bubbles, which are formed almost immediately at the beginning each pulse, act as a low absorption conduit to allow the Er:YAG laser energy to travel deeper into the tissue. The Er:YAG laser only has an optical penetration depth of ~ 10 μm at high temperatures, however the longer pulse duration could allow for the depths of thermal heating measured in the histology. Further detailed studies utilizing a high-speed camera to directly image the cavitation bubble dynamics during mid-IR ablation of both corneal and retinal tissues will be necessary in future work to confirm these claims.

3.4: Multifunctional Scalpel

By integrating multiple functions into a single ophthalmic handpiece the surgeon gains more surgical freedom for simultaneous use of other devices in the otherwise occupied hand. We have improved upon the previous single function microsphere probe by integrating illumination into the otherwise wasted space of the hollow waveguide. Also by making the microsphere scalpel detachable and disposable between procedures, the expensive germanium oxide trunk fiber is preserved and can be re-used. Other instruments commonly used in intraocular surgery could also be integrated with the microsphere scalpel. The most obvious is the vitrector or the suction device used to remove debris from the vitreous. By placing the vitrector tip directly adjacent to the microsphere scalpel (Figure 3.6), any debris created from the ablated tissue or small sections of tissue cut free by the scalpel is instantly removed from the surgical site. We also began work on miniaturizing the microsphere probe to less than 500 µm outer diameters and [34] to be comparable with other 25+ gauge surgical instruments. Figure 3.6 shows an example of a miniaturized microsphere probe created by placing the 200-µm-OD germanium oxide fiber directly in contact with a chain of five 250 µm microspheres.

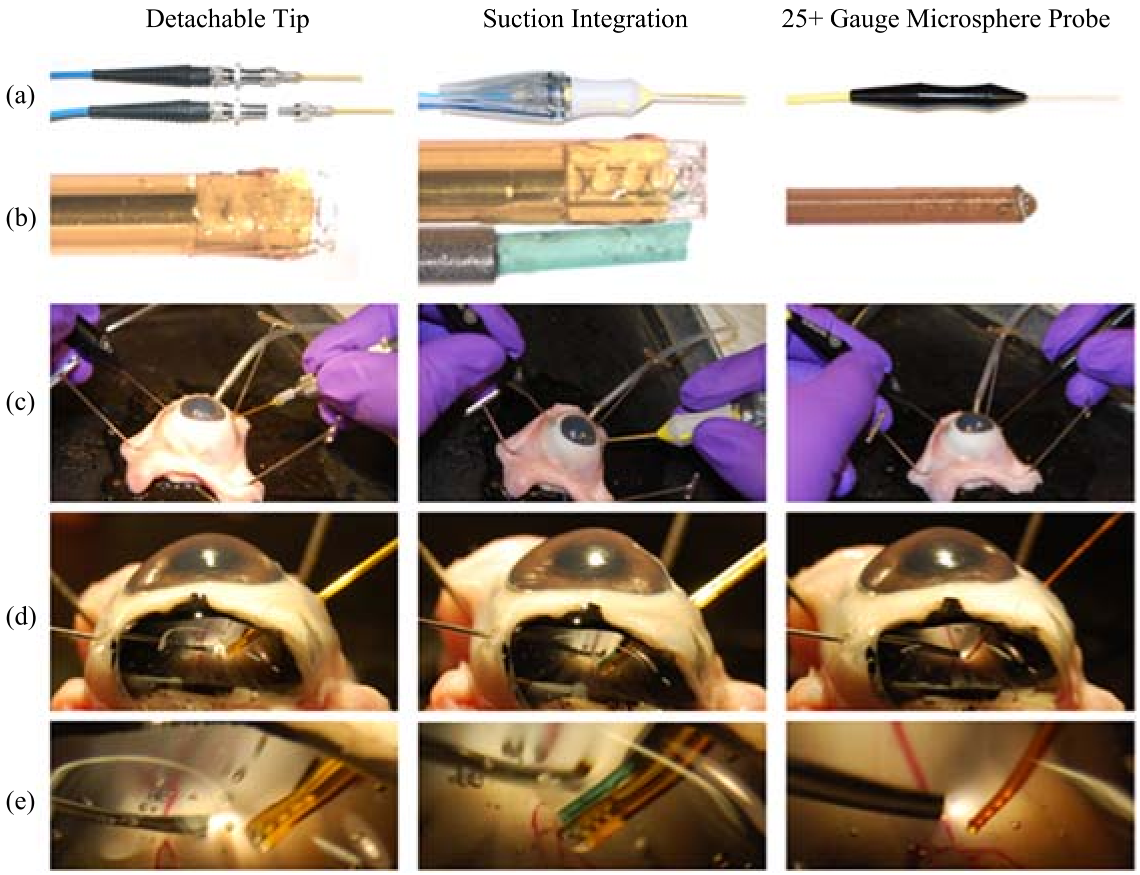

Figure 3.6: The three possible modalities for microsphere scalpel improvement are shown with an additional illumination probe in a retinopathy surgery configuration. (a) Handpiece. (b) Probe Tip. (c) *Ex vivo* intraocular surgical configuration. (d) Cross-section of retinopathy surgery with multifunctional probes (e) magnified.

3.5: Conclusions

Ophthalmic surgery may benefit from use of more precise fiber optic delivery systems during laser surgery. In this study, a laser scalpel consisting of chains of sapphire microspheres positioned at the distal tip of a hollow waveguide was successfully tested on *ex vivo* cornea tissue. One, three, and five microsphere chain structures were modeled, demonstrating a self-limiting short focal depth, especially for the five sphere chain. Single Er:YAG pulses of 0.2 mJ and 75 μs duration produced ablation craters in cornea epithelium for one, three, and five sphere structures with the latter generating the smallest craters with the least amount of thermal damage depth. Microsphere chains produced spatial filtering of the multimode Er:YAG laser beam and fiber, thus providing spot diameters not otherwise available using conventional fiber delivery systems. Integration of other surgical instruments with the microsphere scalpel could improve surgeon familiarity, performance, and eventual adoption. With further development, this novel approach to mid-IR laser ablation may provide an alternative to mechanical tools for surgical dissection and removal of ophthalmic tissues.

CHAPTER 4: DETACHABLE FIBER OPTIC TIPS FOR LASER LITHOTRIPSY

4.1: Background and Overview

4.1.1: Current Laser Lithotripsy Techniques

It is estimated that 10 percent of the United States population at some point in their lifetime will suffer some form of kidney or urinary stone disease. The National Institute of Diabetes and Digestive and Kidney Diseases (NIDDK) reports that for the last two decades, more than 1 million cases occur annually and billions of dollars are spent on evaluations and treatments each year [35].

To treat severe urinary stone disease an endoscopic approach is commonly used with an optical fiber inserted into the working channel of an ureteroscope which stretches from the urethra to the kidney or the stone's location. Initially pulsed dye lasers with pulse durations of nanoseconds or less were used to fragment kidney stones by induced acoustic shockwaves caused by collapsing cavitation bubbles. However, the solid-state, flash-lamp pumped Holmium:YAG laser (Ho:YAG) has become the primary laser used in lithotripsy over the past 15 years. The Ho:YAG laser is currently a favorite among urologists because it can be used to cut or coagulate a variety of soft and hard tissues due to its relatively low cost, high power, and high water absorption at the emission wavelength of 2,120 nm. Instead of fragmenting the stones via a photo-acoustic mechanism like the dye laser, the Ho:YAG's longer pulse duration in the 100's of microseconds regime is predominantly a photo-thermal mechanism [36].

Some limitations of the Ho:YAG laser include a relatively large and multimode beam waist as well as limited flexibility in operating parameters like pulse duration and pulse repetition rate. Due to space limitations in the flexible ureteroscope's working channel which has an inner diameter of ~ 1 mm, fibers with a 270 μm core or less are used for improved irrigation and higher flexibility, especially for accessing hard-to-reach locations such as the lower pole of the kidney. However, coupling into these smaller core fibers with the Ho:YAG laser's multimode beam profile risks overfilling of the input fiber core, launching into the cladding, and damaging the fiber. The large beam waist of the Ho:YAG laser limits optimal power coupling into only optical fibers with core diameters greater than approximately 270 μm (Figure 4.1) [37]. Thermal lensing is also a concern when using the Ho:YAG laser, potentially leading to misalignment of the laser beam with the fiber input end [38]. The short bending radii in the distal end of the flexible ureteroscope further decreases the longevity of fibers with 270 μm core diameters due to laser energy leaking from the core into the cladding and possibility damaging the ureteroscope. Suboptimal coupling from the large multimode beam profile and stone fragmentation can damage the fiber on the proximal and distal ends, respectively, during or after each procedure and the fiber must be repaired or replaced.

Single use and reusable connectorized fibers are available for purchase by surgeons for Ho:YAG laser lithotripsy, with 270 μm and 365 μm core diameter fibers being the most common for use in flexible or semi-rigid ureteroscopes, respectively. Reusable fibers have their jacket stripped, tip cleaved, and are sterilized after each procedure. This reprocessing cost is minimal compared to the cost of a single use fiber. Reusable fibers are usually discarded when they become too short to reach the kidney or if they are irreparably damaged from bending or suboptimal coupling. Reusability of optical fibers for Ho:YAG laser lithotripsy has been shown to decrease single procedure cost by an average of ~ $100 [39].

4.1.2: Thulium Fiber Laser Lithotripsy

The experimental Thulium fiber laser (TFL) has recently been studied as an alternative laser lithotripter to the clinical Ho:YAG laser for several reasons [40-45]. First, the TFL has a higher absorption coefficient (~ 12 mm^{-1}) and shorter optical penetration depth in water, which translates into an approximate 4 times lower ablation threshold for the TFL compared with the Ho:YAG (~ 3 mm^{-1}) [24, 44, 46]. This allows the TFL to ablate tissues at pulse energies much lower than with the Ho:YAG. Although kidney stones have minimal bound water content compared to soft tissues, experiments have shown a wavelength dependant correlation in ablation threshold to water absorption between Ho:YAG and TFL [42]. The TFL has two major emission wavelengths at 1,908 and 1,940 nm which closely match both a high and low temperature water absorption peak, respectively (Figure 4.2). As water heats up during laser ablation, its absorption peak shifts to a shorter wavelength from about 1940 nm at room temperature to about 1910 nm at higher temperatures encountered during laser tissue ablation [24, 47, 48]. It should also be noted that the urinary stone is in a fluid environment and saline irrigation is also used during the procedure to improve visualization, so unbound water is also present at the ablation site.

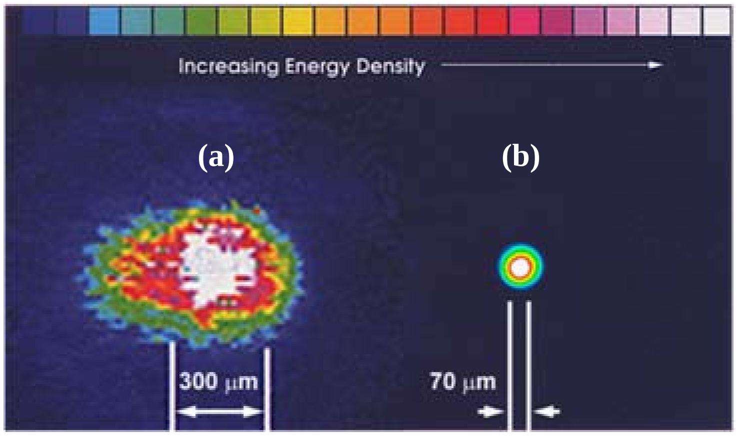

Figure 4.1: Spatial beam waist profiles for (a) Ho:YAG laser (300 µm) on the left, and (b) Thulium fiber laser (70 µm) on the right. Unlike the TFL beam, the multimode Ho:YAG laser beam typically overflows 150 and 200 µm core fibers [37].

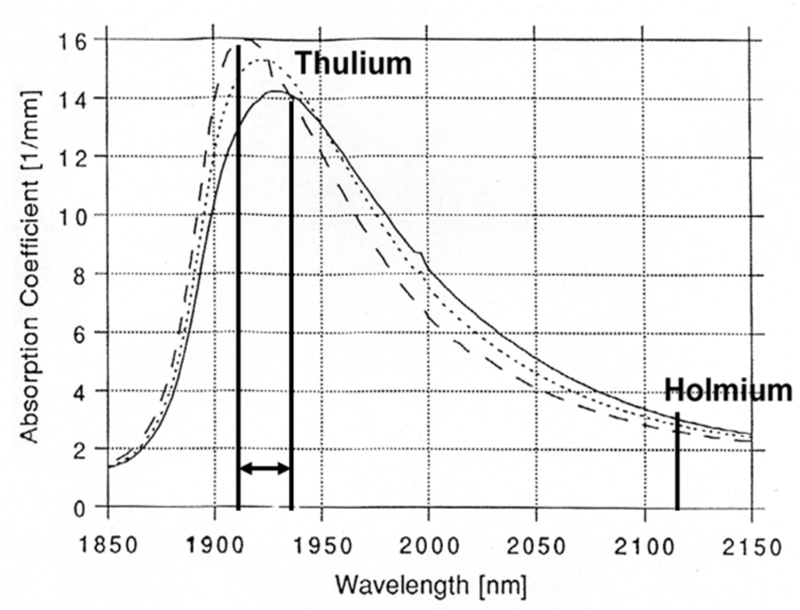

Figure 4.2: The TFL room temperature water absorption peak at 1940 nm shifts to about 1910 nm at ablation temperatures. The major emission lines of the TFL at 1908 and 1940 nm match this shifting peak more closely than the Ho:YAG laser (2120 nm) [47].

The diode-pumped TFL can be electronically triggered to operate at nearly any pulse length or pulse configuration, unlike the flashlamp-pumped Ho:YAG. Micro-pulse trains, or pulse packets, have been shown to increase ablation rates in tissue [49], and lithotripsy [45].

High energy laser pulses are known to create cavitation bubbles, rapidly expanding and collapsing vapor bubbles on the order of a few microseconds, in water. The cavitation bubbles are believed to provide a conduit for the subsequent laser energy to reach the stone with little absorption; however, they may also cause stone retropulsion. Retropulsion is an undesirable side effect that pushes the stone away from the fiber tip during lithotripsy. The bubbles are larger than the diameter of the fiber and can extend from the fiber tip up to ~ 2 millimeters depending on pulse rate and energy. The mechanical shockwaves created by the cavitation bubbles are not believed to be a significant contributor to stone fragmentation at longer laser pulse durations, in the hundreds of microseconds. At pulse durations of 500 μs, the mechanism for ablation is predominantly photo-thermal [50].

Another advantage of the TFL is the Gaussian-like spatial beam profile as compared to the multimode beam of the Ho:YAG laser. The improved spatial beam profile of a fiber laser improves the coupling and transmission of laser power through small-core fibers for lithotripsy, allowing the use of core diameters less than 200 μm [41]. This reduction in fiber cross-section allows for increased flexibility of the ureteroscope and increased saline irrigation rates through the working channel [43, 51], which in turn may reduce procedure times, increase patient safety, and reduce the probability of ureteroscope damage. However, smaller diameter distal tips have been shown to mechanically degrade and suffer from "burn-back" more rapidly than larger diameter fiber tips [43, 52].

4.1.3: Tapered Distal Fiber Tips

Tapered fibers have a core diameter that changes linearly along its length. The taper can be gradual along the entire length of the fiber or steep at one of the tips. Proximal tapered fiber tips have been used to more efficiently couple power from the Ho:YAG laser into a fiber with a small trunk diameter. This typically results in the creation of higher order modes once the small core size is reached at the distal end of the taper. These modes fall outside the total internal reflection condition of the fiber and escape into the fiber cladding, potentially degrading the integrity of the fiber. At short bending radii, these leaking modes may increase, escape, and burn through the ureteroscope wall permanently damaging the expensive ureteroscope and potentially harming the patient.

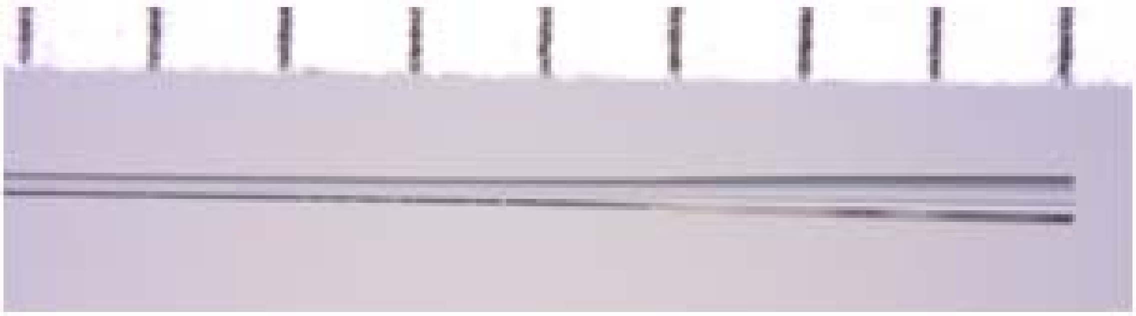

Figure 4.3: Tapered fiber distal tip used for comparative studies. Core diameter increases from 150 to 300 µm over 5 mm. Scale in millimeters.

The Thulium fiber laser, however, provides a unique opportunity for more efficient laser lithotripsy. The Gaussian beam profile allows for improved coupling into small core diameters essentially eliminating proximal fiber tip damage [41]. By reversing the typical orientation of the tapered fiber, and using the increasing taper and larger core at the output, the distal tip is more robust and resistant to damage during the lithotripsy procedure [43]. The benefits of a small core trunk fiber including increased irrigation and flexibility are now combined with those of a large core distal tip for robustness. A steep tapered fiber with a large distal fiber tip, shown in Figure 4.3, can be extruded from the tip of the ureteroscope into contact with the stone for ablation, while also allowing for improved irrigation since only the small diameter trunk fiber remains in the working channel. Other possible advantages of a tapered distal tip include less divergence of the output beam and a larger treatment area on the stone. However, damage and "burn-back" may still occur at the large distal tip and the entire optical fiber must be replaced or repaired during or after surgical procedures. Since the TFL minimizes damage due to coupling at the proximal end, a detachable and disposable large-core distal fiber tip may improve fiber longevity, procedure performance and customization of laser lithotripsy. This study demonstrates similar performance between the previously studied tapered distal fiber tip [43] and a novel small-core trunk fiber to large-core detachable fiber tip design for TFL lithotripsy.

4.1.4: Detachable Fiber Tips

Fiber-to-fiber connectors have been available for decades and are standard in the telecommunications industry. FC, SMA and other fiber connectors have also been used in laser medicine to easily replace and self-align the proximal end of an optical fiber with the laser system for surgical applications. Proximally connectorized fibers are commercially available with cleaved, tapered, diffusing, or side-firing distal tip geometry for surgeons to use intravenously or in conjunction with an endoscope. However, standard fiber-to-fiber connection joints or mating sleeves are too large in diameter and too rigid to exist within a flexible endoscope. To join two fibers or attach a large core distal fiber tip with a low profile less than 1 mm in diameter, splices, capillary and hypodermic tubing have been used. However, these methods are essentially permanent with no way to manually detach and replace tips easily like the large standardized connectors. A small air gap between the two fibers has also shown to reduce coupling damage for high power applications [53]. This study introduces a novel, low-profile, easily detachable, distal fiber tip interface for potential use in laser lithotripsy. A prototype device was designed, constructed, and tested in the laboratory.

4.2: Materials and Methods

4.2.1: Laser and Tapered Fiber

A 100 W Thulium fiber laser (Model TLR 110–1908, IPG Photonics, Inc., Oxford, MA) with a center wavelength of 1,908 nm was used in these studies. The maximum laser output pulse energy used was measured at 42.2 mJ with a power meter (Powermax PM10, Coherent, Santa Clara, CA). The average power measured was divided by the number of pulses per second to obtain the pulse energy. A 75-mm-focal-length calcium fluoride (CaFl) lens was used to focus the 5.5-mm-diameter collimated fiber laser beam down to a spot diameter of approximately 75 µm ($1/e^2$), for coupling into the 150-µm-core trunk fiber of the detachable fiber system and the tapered fiber. The custom 2-m-long tapered fiber, used for comparative studies, has a 150-µm-core to 300-µm-core taper over a 5-mm-length at the distal tip (FIPE150165195, Polymicro, Phoenix, AZ), shown in Figure 4.3.

The laser was electronically modulated with a function generator (DS345, Stanford Research Systems, Sunnyvale, CA) to produce various pulse rates and profiles for device performance testing during stone ablation. For these studies, 500 µs pulses at standard pulse rates of 50 and 100 Hz were compared to 10 and 20 Hz pulse packets consisting of 5 500 µs pulses with 50% duty cycle. These 4 pulse profiles are shown in Figure 4.4a and will be referred to as 50 Hz, 100 Hz, 10 Hz (Packet), and 20 Hz (Packet). The 50 Hz and 10 Hz (Packet) have the same number of total pulses per second, as does the 100 Hz and 20 Hz (Packet), but micro-pulse trains have been shown previously to increase stone ablation rates [45]. Figure 4.4b shows the measured laser temporal pulse profile of the pulse packet. The laser does exhibit a short ramp up and cool down, or “shark-fin” shaped temporal pulse, however, this is common to most trigger pulsed lasers. All the pulses in the packet are still distinguishable and the pulse widths in the trigger pulse are maintained.

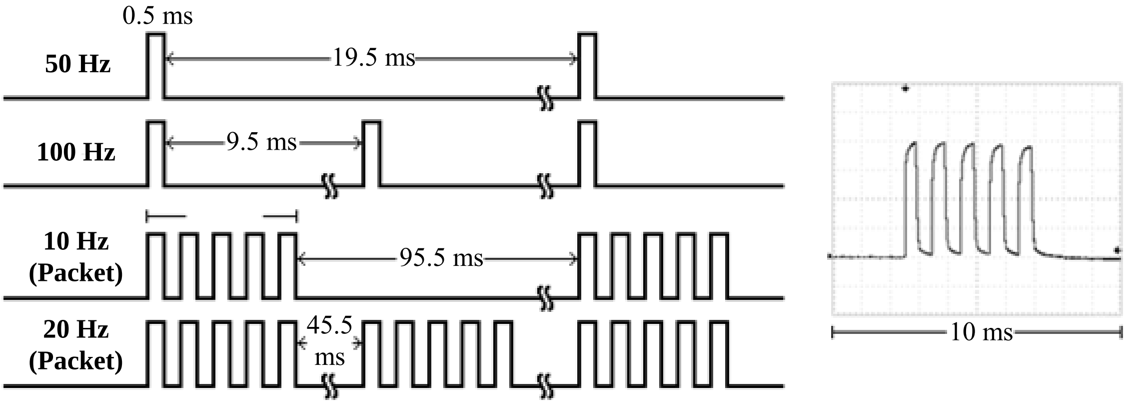

(a) (b)

Figure 4.4: (a) Diagram of pulse trigger structures by function generator. (b) Measured output temporal pulse profile of 50% duty cycle 500 μs pulse packet.

4.2.2: Detachable Fiber Tip Design

Three major constraints were considered when designing the detachable fiber tip interface. First, the design must be approximately 1 mm, or smaller, in diameter to fit into the working channel of a standard flexible ureteroscope. Second, the detachable mechanism must be simple and not time consuming for a urologist to manually perform in the clinic. Third, the design must be practical with a straight forward approach to fabrication and the potential to be mass produced at low cost.

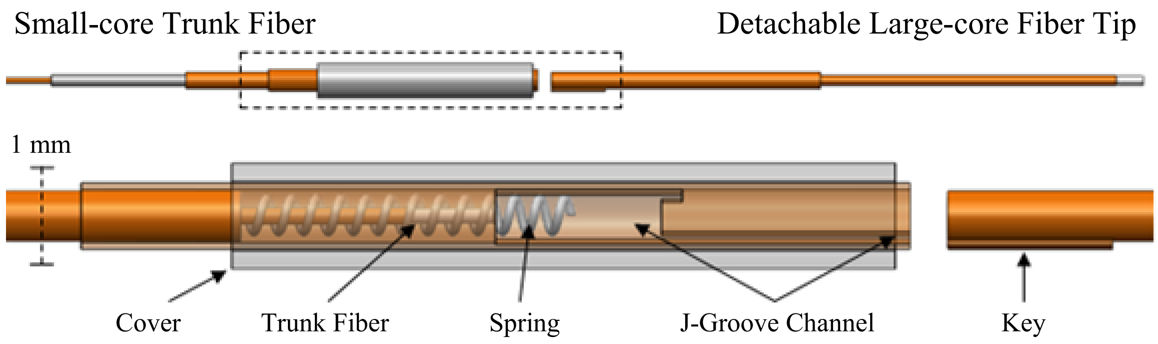

Figure 4.5: Detachable fiber tip design with twist locking mechanism. The trunk fiber contains the locking mechanism while the distal tip is simply outfitted with a keyed sleeve. (Top) Overall interface and detachable tip. (Bottom) Magnified twist locking region with transparent tubing to see internal geometry.

A spring loaded, twist-locking design, shown in Figure 4.5, was invented and chosen for prototyping because it satisfied all of the design constraints. A trunk fiber was fitted with a small compression spring with a 600 and 400 µm outer and inner diameter, respectively. This spring became the main dimensional constraint of the design as it was the smallest commercial compression spring available. The dimensional designs were based on a low-OH silica trunk fiber with a 150-µm-core-diameter and a length of 2 m, which was chosen because it has identical trunk fiber characteristics as the custom tapered fiber for comparison. The fiber tips were of the same material and manufacturer and had core diameters of 300 µm. Based on these three parts, inexpensive hypodermic stainless steel and polyimide tubing of various sizes was cut and shaped to suit the two fibers and spring and provide concentric structure. The key on the detachable tip was made from 36 gauge wire. Table 4.1 summarizes the components and their dimensions used to construct the detachable tip prototype. Appendix B further details the detachable tip assembly procedure.

Table 4.1: Materials used to assemble detachable fiber optic tip prototype. All dimensions for inner (ID), outer diameter (OD), and cut length are in millimeters.

	Part	ID	OD	Length	Part #
Trunk	Fiber	n/a	0.195	2000	FIP150165195 (PM)
	Tubing (S)	0.203	0.414	50	B00137POT6 (AS)
	Tubing (P)	0.455	0.607	40	B000FN4422 (AS)
	Spring	0.400	0.600	4	CIM010ZA 05S (LS)
	J-groove Tubing (P)	0.643	0.795	25	B0013HUD9M (AS)
	Cover Tubing (S)	0.838	1.270*	20	B000FN0VNS (AS)
Tip	Fiber	n/a	0.370	50	FIP300330370 (PM)
	Tubing (P)	0.455	0.607	15	B000FN4422 (AS)
	Key	n/a	0.125	2.5	Wire-MW-36-1/4 (PW)

Materials: (S) Stainless steel, (P) Polyimide
Manufacturer: (PM) Polymicro, Phoenix, AZ, (AS) Amazon Supply, Seattle, WA,
(LS) Lee Spring, Greensboro, NC, (PW) Powerwerx, Brea, CA
*Filed down to an outer diameter of approximately 1.000 mm

All fiber tips were polished on both ends using 0.3-μm-grit aluminum oxide polishing pads (Buehler, Lake Bluff, IL). All the components were sealed and glued with super glue (Loctite, Westlake, OH). Only one piece of tubing in the design needed to be machined beyond just cutting to length or hand filing, and that was the J-groove that needed to be machine carved to provide a channel for the key, shown in Figure 4.6. A 125-μm-diameter end mill bit (05EM013-2-070FL, Drill Bit City, Prospect Heights, IL) in conjunction with a MicroLux tabletop vertical milling drill (Micro-Mark, Berkeley Heights, NJ) was used along with x-y-z micromanipulation stages under magnification to cut the J-groove channel in the hypodermic tubing. The design provided a small air gap between the trunk fiber and the distal fiber tip, controlled by the length of the locking notch in the J-groove which was approximately 0.3 mm. The fiber tip had to remain within a minimum distance from the trunk fiber so the divergence of the trunk fiber did not overfill the fiber tip. The stainless steel cover, which was originally 1.27-mm-outer-diameter, was filed down to approximately 1.00-mm-outer-diameter in a drill, operating like a lathe, to fit inside a typical flexible ureteroscope's 1.19-mm-inner-diameter working channel.

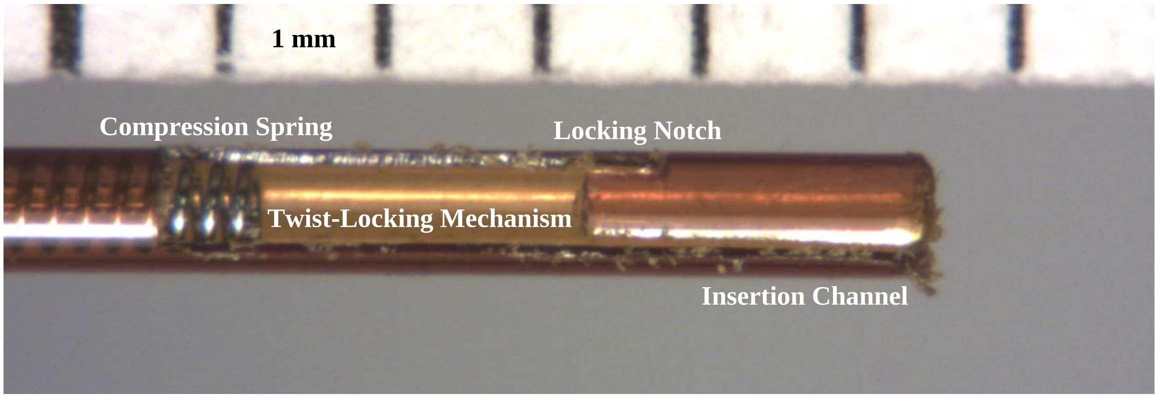

Figure 4.6: Photograph of detachable fiber tip twist-locking mechanism or "J-groove" with outer cover removed.

With the trunk fiber tip barely recessed beyond the J-groove cut and the proximal end of the detachable tip flush with the edge of the locking key, the trunk to tip air gap was approximately 0.3 mm, or the length of the locking notch. The overall insertion distance of the tip was approximately 5 mm followed by a 0.3 mm return after 90 degree clockwise rotation and release. The detachable tip mechanism that fell above the 200-µm-outer-diameter trunk fiber, shown in Figure 4.8a with the tip attached, had an overall length of approximately 100 mm with only about 20 mm of that region rigid around the fiber interface, with an overall outer diameter of 1 mm. The polyimide tubing and the thin steel tubing on the trunk fiber were flexible. The entire detachable system was deflected up to 45 degrees without transmission failure, demonstrating the robust alignment of the trunk/tip interface.

4.2.3: Optical and Thermal Characterization

Transmission efficiency tests were performed by measuring pulse energy at locations before the trunk fiber and after the distal tip, for both detachable and tapered fibers, using a power meter. A thermal imaging camera (Thermovision A20M, FLIR Systems, Boston, MA) was used to obtain a temperature profile of the detachable fiber tip interface and the tapered fiber during laser emission. Spatial beam profile measurements were acquired by focusing the fiber tip's surface with a 0.5 NA CaFl magnification lens (ISP Optics, Irvington, NY) onto a beam profiler (Spiricon Pyrocam III, Ophir, Logan, UT). The beam profiler was also used without a magnification lens at incremental distances to analyze the numerical aperture (NA) of each fiber tip. If the device was used in surgery, the fiber would be under constant random manipulation by the surgeon. Since the output spatial beam profile was highly dependent on the fiber length and bend configuration, subtle motion was induced along the length of the trunk fiber and an average spatial beam profile was taken over a period of 10 seconds.

4.2.4: Lithotripsy Setup

To compare the stone ablation performance of the detachable fiber tip to recent tapered fiber studies, human calcium oxalate monohydrate (COM) urinary stone samples with >95% purity were obtained from a stone analysis laboratory (Louis C. Herring & Co, Orlando, FL). The stone samples ranged in diameter from 8 to 15 mm and in mass from 150 to 500 mg with an average mass of about 250 mg. The initial dry stone mass was recorded with an analytical balance (AB54-S, Mettler-Toledo, Switzerland) before securing the stone in place with a clamp and then submerging it into a saline bath. Figure 4.7 shows the stone testing experimental setup. The laser radiation was delivered through the prototype detachable tip or a tapered fiber to the stone surface in contact mode. An output pulse energy of approximately 30 mJ was used with both fibers. The higher transmission of the tapered fiber required the laser to be operated at a slightly lower power to compensate. The fiber was held manually and a scanning motion over the stone surface under gentle force was used during pulsing to keep the fiber in contact with the stone's surface. A total of 6000 pulses was delivered to each stone sample, translating into stone ablation for 1 or 2 minutes for 100 or 50 pulses/sec, respectively. The stones were then dried in an oven at 70°C for over 30 minutes before final dry mass measurements.

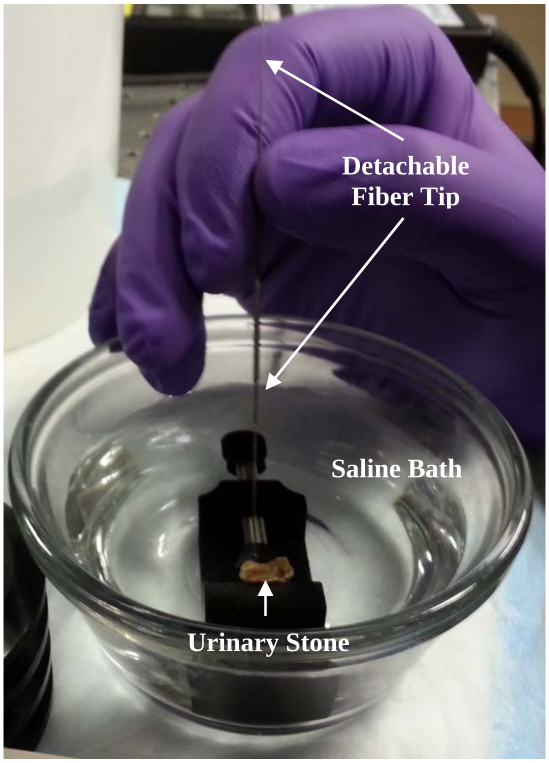

Figure 4.7: Laser lithotripsy setup consists of a human COM urinary stone submerged in a saline bath with the detachable fiber tip or the tapered fiber tip held manually in contact with the stone surface during laser irradiation.

4.2.5: Fiber Tip Degradation

The primary motivation for using detachable fiber tips is the observation that the distal tip degrades or experiences “burn-back” during stone fragmentation. Two fiber degradation studies were performed to better understand the trends and possibly the cause of fiber “burn-back.” First, microscopic images of the distal fiber tips were taken after stone ablation to analyze trends in “burn-back” as a function of laser pulse rate and temporal pulse configuration. The detachable fiber tips and the tapered fiber were illuminated with a white lamp from the proximal end. The detachable fiber tips also provided a unique opportunity to compare fiber tip roughness to number of pulses during stone fragmentation because short length fiber tips in a vertical orientation could easily fit under and be measured with a commercial tabletop interferometer nominally used for polished mirrors, flats, or lenses. Surface roughness measurements were performed using a scanning white light interferometer, SWLI, (ZeGage, Zygo Corporation, Tucson, AR) using a 50x magnification objective. A spherical fit to the profile was removed because the fiber tips were slightly convex due to the fiber polishing machine. A 150-µm-length measurement profile, and/or cropped area was drawn in the software away from obvious singular features, dust or pits, to achieve a representative roughness of the fiber’s core surface. The fiber was initially polished and measured, then re-measured after stone fragmentation to analysis fiber tip roughness.

4.3: Results

4.3.1: Optical and Thermal Measurements

For the detachable fiber tip the measured input and output pulse energy was 38.4 and 30.7 mJ, respectively, yielding a 79.9% transmission. The tapered fiber measured 35.2 mJ for the same input energy, yielding a 91.7% transmission. The detachable fiber tip had four silica / air interfaces while the tapered fiber tip only had two. The theoretical optical transmission rates of the detachable and tapered fiber tip were calculated to be 87.3% and 93.3%, respectively. The theoretical transmission was based on a Fresnel reflection loss of 3.25% at each silica (n=1.44) / air (n=1) interface and 0.014 dB attenuation through 2-meter-long fiber at λ = 1908 nm.

Table 4.2 shows a device heating analysis performed by lateral thermal imaging and temperature measurement of the detachable tip mechanism and the tapered distal fiber tip during laser emission. Figure 4.8 shows thermal images taken of detachable and tapered fiber tips during laser operation with 30 mJ at the different pulse configurations. Scaled based on pulse configuration, all thermal images showed heating at the same locations along the fiber length. Temperature rise in both fibers was dependent on total pulses per second rather than pulse configuration, standard or packets.

Table 4.2: Peak temperature and temperature rise (°C) of detachable and tapered fiber tips as a function of laser temporal pulse profile. Mean room temperature for detachable (24.6°C) and tapered (24.9°C) fiber measurements. Pulse energy: 30±2 mJ.

		Detachable Tip		Tapered Tip	
Pulse Profile	Pulses/sec	Interface	Distal Tip	Trunk	Distal Tip
50 Hz	50	30.1 (Δ5.5)	36.1 (Δ11.5)	26.0 (Δ2.6)	25.3 (Δ1.9)
10 Hz (Packet)	50	27.8 (Δ3.2)	37.4 (Δ12.8)	26.1 (Δ2.7)	25.9 (Δ2.5)
100 Hz	100	31.2 (Δ6.6)	48.5 (Δ23.9)	28.4 (Δ5.0)	27.3 (Δ3.9)
20 Hz (Packet)	100	33.5 (Δ8.9)	47.0 (Δ22.4)	28.7 (Δ5.3)	27.8 (Δ4.4)

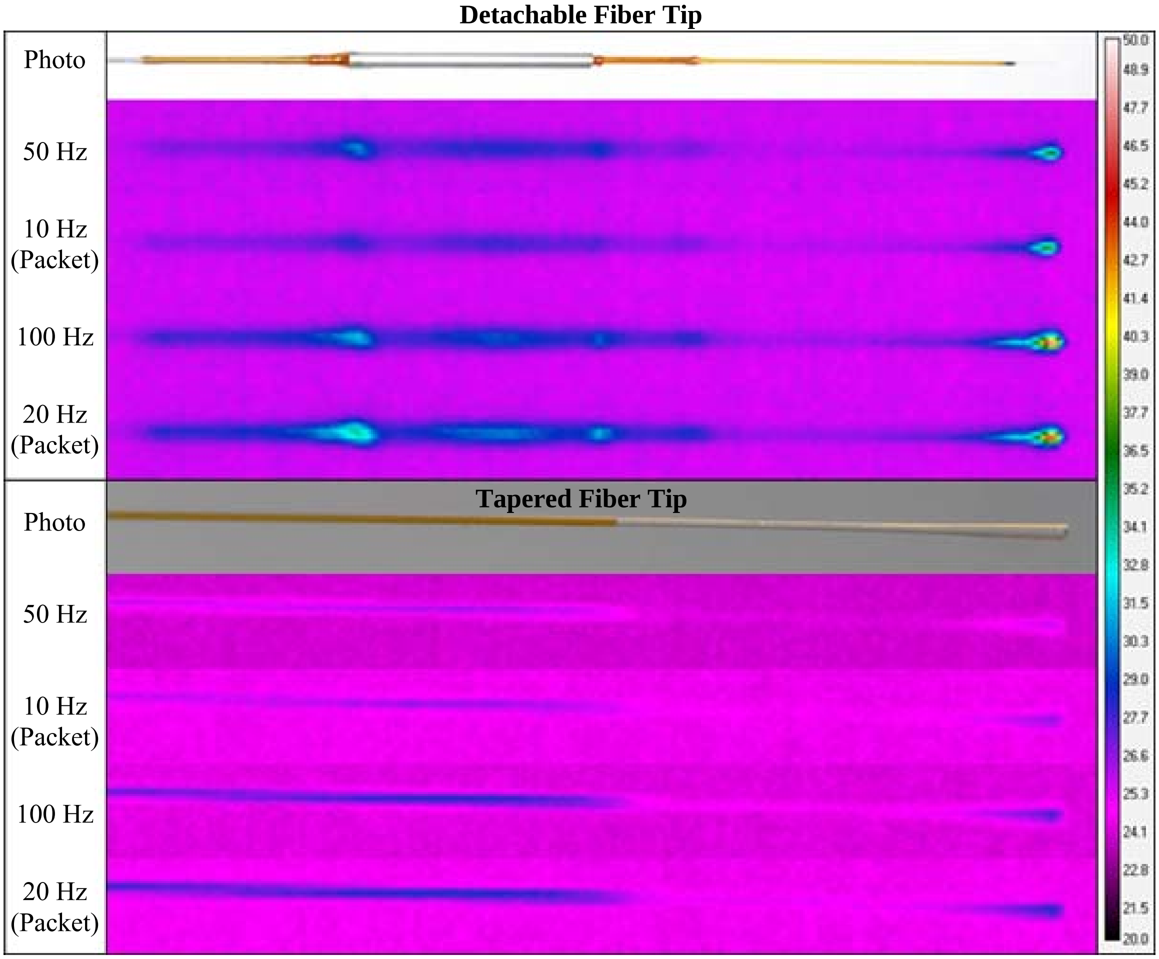

Figure 4.8: (Top) Photograph of detachable fiber tip prototype with thermal images in air operating at 30 mJ pulse energy. Horizontal image width 100 mm. (Bottom) Tapered fiber tip with thermal images in air, image width 25 mm.

Spatial beam profiles magnified at the fiber tip's surface for the 150-to-300-µm-core-diameter detachable fiber tip and the similar sized tapered fiber are shown in Figure 4.9. The detachable tip displays a Gaussian-like profile while the tapered fiber has a more unique profile with rings. An experimental numerical aperture was calculated by measuring beam radii at various distances from the distal fiber tip using a spatial beam profiler. With the proximal fiber launching condition kept common at ~ NA=0.037, the detachable and tapered fiber tips had output NAs of 0.078 and 0.055, respectively.

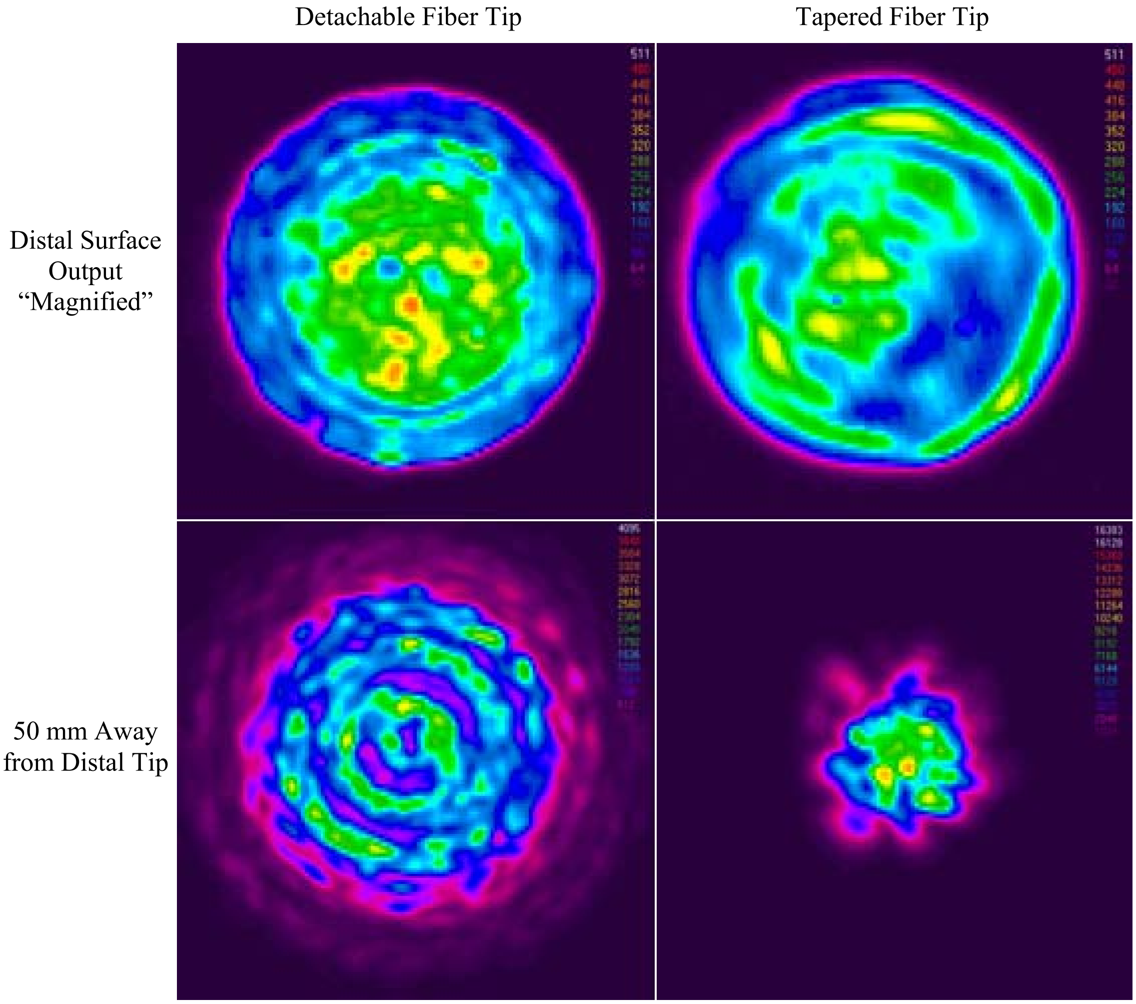

Figure 4.9: Spatial beam profiles for detachable and tapered fiber tips. (Top row) Magnified 300 µm core diameter distal fiber tips. (Bottom row) 50 mm away from distal fiber tip with box size 12.4 x 12.4 mm.

4.3.2: Lithotripsy

COM stones were successfully ablated with the detachable fiber tip at a maximum rate of 187 µg/s using the 20 Hz (Packet) pulse profile at 30 mJ. Table 4.3 shows the mean ablation rate based on five stone samples for each set of laser parameters. The stones were not fragmented into smaller stones by the laser. All stone mass loss was the result of stone ablation or ejection of microscopic stone dust. Contrary to the temperature rise results, stone ablation rate for both fibers tends to favor the pulse packets rather than the standard pulse rates. A Student's t-test showed no statistical difference between the detachable and tapered fiber stone ablation rates.

Table 4.3: COM stone ablation rates (µg/s) for detachable and tapered fiber tips as a function of laser pulse rate and profile. Rates calculated from mass loss after 6000 pulses (N=5). Pulse energy: 30±2 mJ.

Pulse Profile	Pulses/sec	Detachable Tip	Tapered Tip
50 Hz	50	50 ± 15	47 ± 9
10 Hz (Packet)	50	108 ± 13	94 ± 22
100 Hz	100	113 ± 8	92 ± 37
20 Hz (Packet)	100	187 ± 37	175 ± 31

Thulium fiber laser lithotripsy with low pulse energies and high pulse rates resulted in stone vaporization or "dusting" with very small particles created, rather than fragmentation into larger stone pieces. The laser stone vaporization approach may offer some advantages compared to fragmentation because the residual stone particles or dust are small enough to be naturally passed on their own, and unlike larger stone fragments, would not require use of a stone basket to retrieve fragments and ensure that the patient is stone-free. Further investigations comparing laser stone vaporization to fragmentation are warranted.

4.3.3: Fiber Tip Degradation

Fiber tip degradation for the detachable fiber tip was studied in two ways. First, the microscopic images of the fiber tips after stone ablation are shown in Figure 4.10. Minimal degradation is seen for 50 Hz, while 100Hz and the 10 Hz (Packet) start to show signs of pitting. Significant "burn-back" is seen at 20 Hz (Packet) for both detachable and tapered fiber tips. This trend is consistent with the stone ablation rates. Second, to better understand the "burn-back" mechanism a more rigorous fiber tip roughness analysis was also performed. Figure 4.11 and Table 4.4 shows the measured fiber tip roughness before and after the delivery of 60,000 total laser pulses at 50 Hz. This is equivalent to 20 minutes or 5 times longer stone ablation than the 12,000 pulses tip degradation image for 50 Hz in Figure 4.10. All of the common roughness parameters showed no change, within uncertainty.

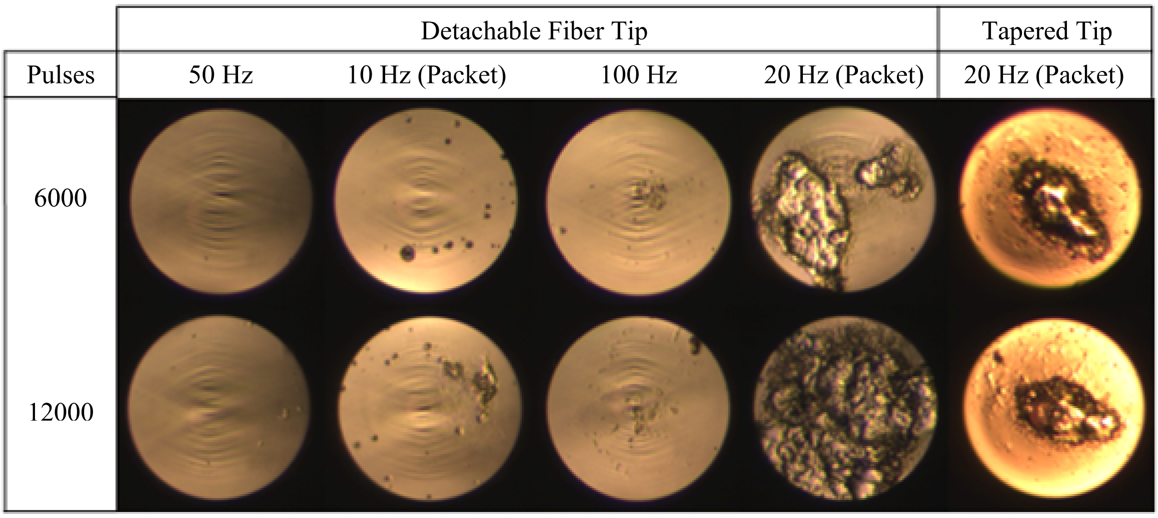

Figure 4.10: Distal fiber tip degradation as a function of pulse profile and total number of pulses. All fiber tips were held manually in contact with the stone during laser irradiation with 30 mJ pulse energy. Considerable fiber tip degradation was observed using the 20 Hz (Packet) for both fibers.

Table 4.4: Surface (S) and line profile (R) roughness measurements. Comparison of polished fiber, before and after 60,000 500-μs pulses at a standard pulse rate of 50 Hz with a pulse energy of 30 mJ. All dimensions are in nanometers.

Parameter		Before	After
Peak-Valley	Spv	1638.60	1637.80
RMS	Sq	9.77	7.02
Average	Sa	3.60	5.12
Peak-Valley	Rpv	50.03	52.51
RMS	Rq	4.86	5.52
Average	Ra	3.45	4.32

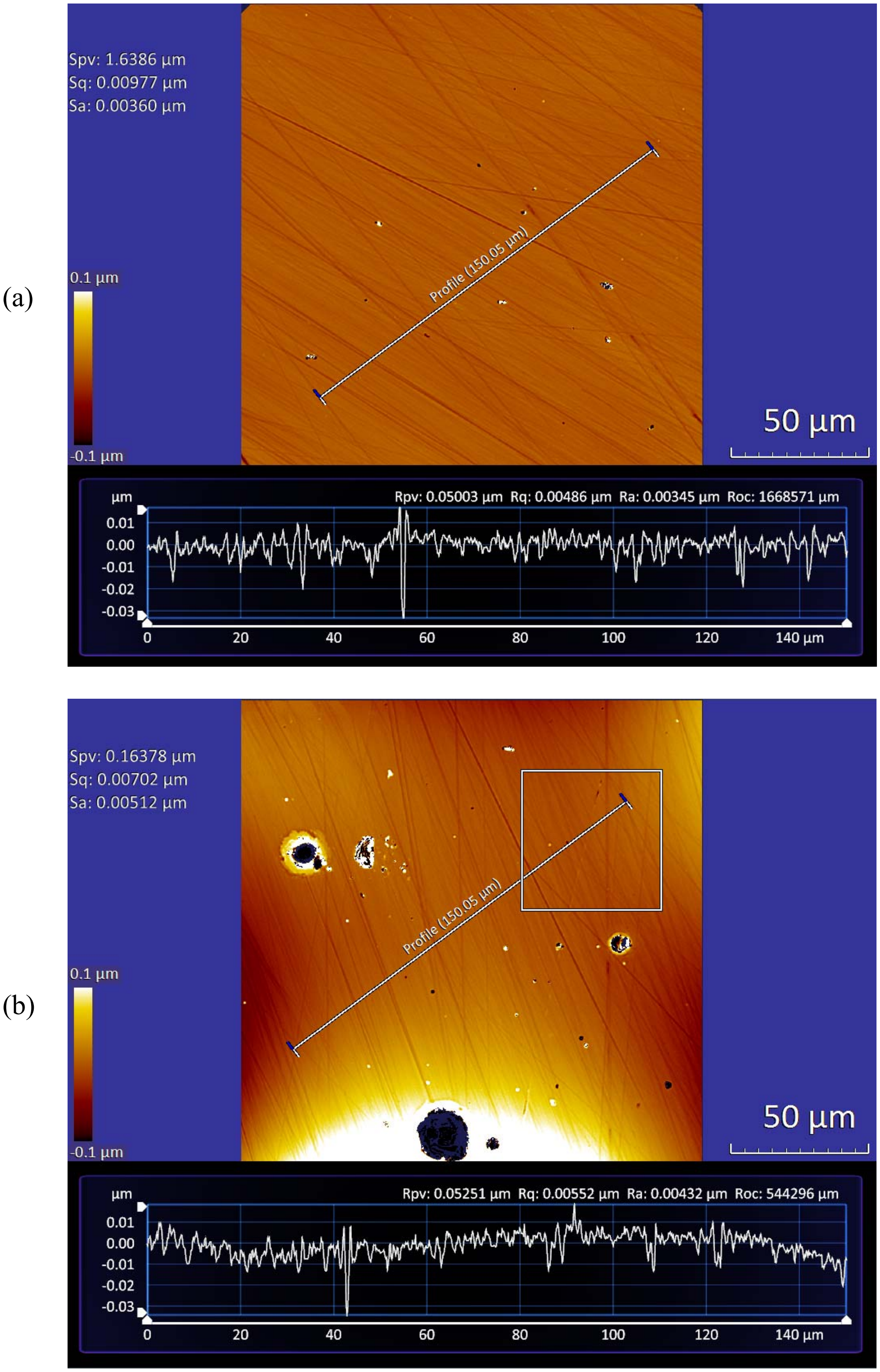

Figure 4.11: Distal fiber tip roughness measurement using a scanning white light interferometer. (a) Polished and before lasing. (b) After 60,000 500-µs pulses at a standard pulse rate of 50 Hz with a pulse energy of 30 mJ. Surface roughness measurements are from 50 x 50 µm cropped area, away from burns or pot marks.

4.4: Discussion

4.4.1: Detachable Fiber Tip Design

The detachable fiber tip prototype has a much smaller diameter and is more flexible than commercial fiber connectors. The current overall device diameter of 1.00 mm (3.0 French) is slightly smaller than a typical flexible ureteroscope's working channel diameter of 1.19 mm (3.6 French). However, the design itself could easily be scaled down further if a smaller spring was available. The large length of the current prototype was to aid in the manual grasping of the device in the *ex vivo* stone ablation testing, shown in Figure 4.8. If the J-groove part was reduced in diameter, it would need to be machined from stainless steel tubing. The polyimide tubing would be too flexible at these small diameters and the J-groove cut would need to support the pressure of the spring and multiple tip exchanges with consistency. The cut lengths of all the device components, shown in Table 4.1, could be reduced increasing the overall flexibility for use inside the ureteroscope's working channel, and so that the fiber could be inserted through the working channel during the procedure without hindering ureteroscope deflection. The cyanoacrylate-based "superglue" used in this preliminary study could also be replaced by a heat-resistant biocompatible glue, thus making it acceptable for clinical use and re-sterilization, if necessary.

4.4.2: Optical and Thermal Analysis

Both the detachable and tapered fiber tips performed within 90% of their theoretical transmissions. Minor discrepancies may lie in the proximal coupling, polishing artifacts, or in the case of the detachable fiber tip, debris from construction or suboptimal concentricity between the trunk and tip fibers.

Table 4.2 shows temperature rise in both fibers was a function of total pulses per second rather than the pulse configuration. The detachable fiber tip device did not reach a surface temperature above 50°C which could be potentially harmful to the patient if in contact with soft tissues. The heat generated at the detachable distal fiber tip was believed to be the result of an inadvertent slightly angled tip surface, which resulted from polishing the short length fiber tips in fiber holders designed for much longer fibers. Steeper angled tips divert more back reflection into the cladding of the fiber causing more heat buildup. The tapered fibers were flat polished by the manufacturer. The detachable interface heating was due to the reflections within the air gap region between the two fibers, and the back-reflected light from the distal tip overfilling the trunk fiber. An index-matching fluid would reduce this heating; however, no such fluid which was bio-compatible and also provided a high damage threshold was available. These thermal profiles were taken in air. During lithotripsy, the fibers would be in a saline irrigation environment providing cooling and the distal tip would have a silica / saline interface reducing back reflection, which is believed to be the primary cause of all the undesirable heating. However, both the detachable and the tapered fiber tip would be extruded from the tip of the ureteroscope during stone ablation making the distal tip heating less significant than the detachable fiber interface which could remain inside the ureteroscope's working channel.

The spatial beam profiles, shown in Figure 4.9, taken at the fiber tip surfaces show that the detachable fiber tip does not alter the shape of the Gaussian laser beam profile that was launched into the trunk fiber. However, the width of the beam does increase to better fill the larger tip diameter. This was predicted as there are no beam altering surfaces, only two step-index fibers with identical NA. The far-field beam profiles are of little significance to lithotripsy since the cavitation bubbles are believed to be a conduit for the laser energy to the stone, the divergence or NA might play a small role in energy density as the light reaches the stone surface. However, the tapered distal fiber tip has a smaller numerical aperture than that of the detachable fiber tip. This is due to the change in modal structure and focusing in the tapered region. The spatial beam profiles, like the thermal measurements, were taken in air and therefore the outer ring visible in the tapered fiber profile could be an artifact of the distal fiber tip back-reflection re-encountering the tapered region from the opposite direction and then exiting the fiber tip. In saline this outer ring may be reduced so that the actual spatial beam profile only contains the central region.

4.4.3: Lithotripsy Analysis

Since COM urinary stones are the most common stones, other stone types were excluded from this study where the main purpose is to demonstrate a functional and practical prototype for a detachable fiber tip. Table 4.3 shows an increase in stone ablation rate for both the detachable and tapered fibers when using pulse packets versus standard pulse rates. This is comparable to previous studies with a 100-μm-core-diameter fiber operating at 35 mJ with a pulse width of 500 μs, which demonstrated COM stone ablation rates of 60 and 122 μg/s for 50 Hz and 10 Hz (Packet), respectively [45]. Although in the detachable fiber tip the energy density is less, the same trend of nearly double the ablation rate still applies; the rates are only slightly lower. The technician took added precautions when handling the tapered fibers due to the fact that the tapered region of the fiber is much more delicate and prone to breaking than the detachable fiber tip device. Slight differences in ablation rates between the detachable and tapered fiber tips could be a result of less aggressive and less frequent contact force between the tapered fiber tip and the stone's surface.

4.4.4: Degradation Analysis

Distal fiber tip degradation, shown in Figure 4.10, appears to follow the same trend as the stone ablation rates. The packet configurations degraded the tip faster than the equivalent standard pulse rate. The rapid heating of the fiber tip when in "contact" with the stone using the pulse packets or any high pulse rate could be the cause of the "burn-back."

When a cavitation bubble forms between the tip and stone surface, in contact, the first pulse voids the intermediate region of liquid and the following pulses in the packet arrive before collapse and therefore superheat the fiber tip and stone surface in the steady vapor pocket. When the fiber tip is slightly out of contact, operating at a lower pulse rate, or if the fiber has a smaller diameter, the cavitation bubble can collapse providing cooling to the fiber tip. The previous study with 100-μm-core-diameter fibers showed a decrease in fiber tip degradation or "burn-back" when using pulse packets [45]. The discrepancy in that study can be explained by the difference in ablation crater shapes caused by the pulse packet, which are much wider due to the increased ablation rate. The wider crater combined with the smaller fiber diameter could account for the better cooling. Standard pulse rate craters are more narrow and deep causing the small fiber to descend and get stuck. In these confined craters the cavitation bubbles cannot collapse, superheating occurs, and the fiber degrades faster. The detachable fiber tip has roughly 10 times the surface area of the 100-μm-core-diameter fiber used previously as well as originating from separate manufacturers, therefore the “burn-back” analysis is not directly comparable and a more thorough study is warranted in the future.

The tapered fiber tip showed similar degradation to the detachable fiber tip at 20 Hz (Packet) however it was mostly confined to the central region of the tapered fiber. Assuming the outer ring in the tapered fiber’s spatial beam profile, shown in Figure 4.9, is reduced when operating in a saline environment, the beam central region closely resembled the degradation area of the fiber tip.

The distal fiber tip appeared to experience no or minimal “burn-back” at a standard pulse rate of 50 Hz and therefore minimal heating of the fiber tip. This pulse rate was then used as a control model to observe whether or not the stone fragmentation and bombardment of the fiber tip with stone debris actually degraded the fiber. After 60,000 pulses or 20 minutes of contact stone ablation at 50 Hz the roughness parameters of the fiber tip’s surface, shown in Figure 4.11 and Table 4.4, essentially were unchanged. This result supports the conclusion that the urinary stone material is not abrasive to the silica fiber. Degradation is then primarily caused by the heating of the fiber tip until the silica undergoes a phase change.

4.5: Conclusions

The current clinical laser lithotripter, the Holmium:YAG laser, cannot couple into small core diameter fibers without proximal fiber tip damage and therefore ureteroscope flexibility and irrigation are reduced. This study expands upon the possible benefits of using a Thulium fiber laser, which with its Gaussian spatial beam profile can couple into smaller diameter fibers. With no proximal fiber tip damage, the primary motivation for using detachable fiber tips is the observation that only the distal fiber tip degrades or experiences "burn-back" during stone fragmentation. This study introduced a novel, low-profile, twist-locking, detachable distal fiber tip interface for potential use in Thulium fiber laser lithotripsy. A 1.00-mm-outer-diameter detachable fiber tip interface was designed, constructed, and tested *ex vivo* on urinary stones in the laboratory. Similar stone ablation rates between the previously studied tapered distal fiber tip and the detachable fiber tip were shown. The largest ablation rates were observed when using the pulse packets, however, these higher rates also contribute to the fastest distal fiber tip degradation. For urologists desiring faster TFL lithotripsy procedures, the incorporation of detachable distal fiber tips allows for quick replacement of damaged tips without worrying about the laser to trunk fiber connection. The design could be scaled down further with improvements in materials and manufacturing, or be used with more exotic and expensive mid-infrared trunk fibers. This method for sparing the trunk fiber could be a motivation for integrating a dedicated laser fiber into the ureteroscope itself, with detachable distal tips, freeing the working channel for the use of other surgical instruments.

CHAPTER 5: HOLLOW FIBER TIPS FOR LASER LITHOTRIPSY

5.1: Background

5.1.1: Motivation for Hollow Fiber Tips

The previous chapter concluded that fiber tip degradation was primarily the result of super heating and not the impact of stone fragments. When the distal fiber tip is in contact with the stone, and either operating at a high pulse rate (TFL) or high pulse energy (Ho:YAG), the confined vapor bubble cannot collapse between consecutive pulses. In this instance, the fiber tip could experience melting temperatures (~ 1000°C) which lead to fiber tip degradation. This effect can be observed during stone ablation by a visibly bright flash or sparking when the fiber tip comes in contact with the stone.

Several ways to reduce heating of the fiber tip are to decrease pulse rate, decrease pulse energy, increase fiber tip diameter, or increase the fiber distance to the stone. Decreasing the pulse rate is a viable option; however surgeons would prefer faster procedures by sacrificing fiber tip degradation. Also stone ablation rates appear to stall out dramatically when operating at pulse energies lower than ~ 30 mJ at 500 μs duration, and the laser power was limited to a bare fiber output of ~ 35 mJ. Surgeons currently can solve this problem by increasing the fiber core diameter, however small diameter fibers are desirable due to increased flexibility and irrigation in the working channel of the ureteroscope. With a bare fiber the stone to fiber distance is nearly impossible to control due to stone motion and retropulsion during operation, and ablation stall out has been observed beyond ~ 1 mm due to absorption of the laser energy by the intervening water layer. A hollow tube could be placed over a recessed and fixed fiber tip to control the fiber to stone distance, by simply placing the tube in contact with the stone. Hollow fiber tips could possibly reduce or eliminate fiber tip degradation while still maintaining acceptable stone ablation rates and a small diameter footprint.

5.1.2: Retropulsion and Suction Effect

Water flow surrounding the fiber tip, caused by exploding cavitation bubbles, has previously been studied [54]. In this study, using a bare fiber placed in a water bath containing microspheres as visible scatterers, significant water flow was witnessed in the forward direction along the optical path. This flow increased with increasing pulse rate and energy. Weaker secondary water vortices were seen in the reverse direction, and allowed for pulling of the stone when placing the fiber tangent to the polar region of the stone instead of normal to the equator (Figure 5.1). In this chapter, the retropulsion force of hollow fiber tips are studied along with a novel tip design that could possibly control the cavitation bubbles created at the fiber tip.

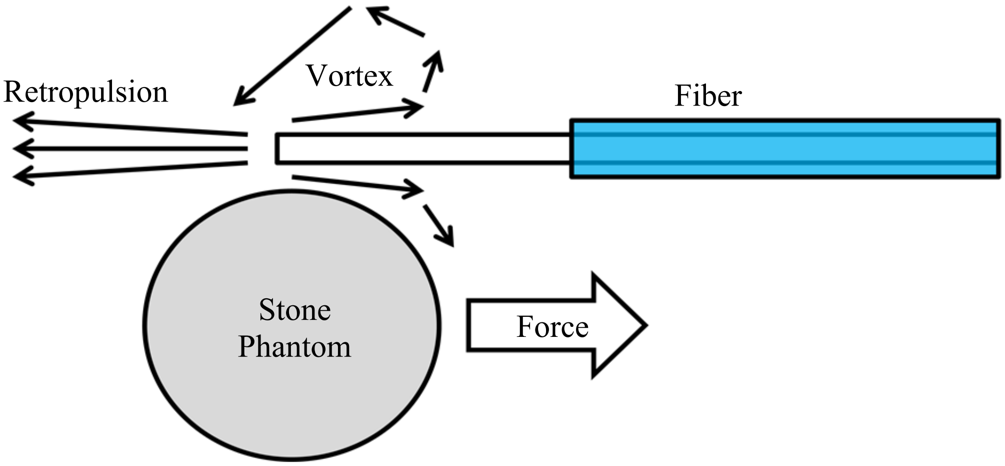

Figure 5.1: Representation of suction effect on stone phantom.

5.2: Materials and Methods

5.2.1: Hollow Fiber Tips

The same trunk fiber used in the previous chapter was also used in this study for direct comparison: a low-OH silica trunk fiber with a core and cladding diameter of 150 and 165 µm, respectively, and a length of 2 meters (Polymicro, FIP150165195). The fiber jacket (195 µm OD), was stripped back ~ 15 mm. Stainless steel hypodermic tubing with an inner and outer diameter of 178 and 356 µm, respectively, cut to a length of ~ 10 mm was used for each hollow tip. A micromanipulator was used to recess the fiber in the tube to a set distance. A small amount of super glue was placed on the back end of the tube to fix the tube and fiber together. A photograph of the hollow fiber tip is shown in Figure 5.2.

Figure 5.2: Photograph of ~ 350 µm OD, 10 mm long stainless steel tube glued to 150 µm core diameter trunk fiber.

The ideal fiber tip recession distance was unknown so various distances were tested including 100 µm which was less than the fiber diameter, up to 1 mm the experimental ablation stall out distance for a bare fiber. The five scenarios tested are shown in Figure 5.3. Before testing it was hypothesized that the vapor bubble could not collapse back into the front of the hollow tip after the initial pulse, possibly allowing for longer fiber-stone separations than with a bare fiber due to reduced attenuation.

Figure 5.3: Scale representation of five fiber tips tested based on fiber recession distance. Length of stainless steel tube: 10 mm.

5.2.2: Retropulsion Study

Polymer microspheres (Duke Standards 4000 Series, Thermo Fisher Scientific, Waltham, Massachusetts) with diameters ranging from 30 to 50 μm, $n \approx 1.59$ for visible light, and density of 0.00105 g/mm^3 were suspended in a water filled Petri dish, Figure 5.4, and was illuminated from the side by a white fiber-optic lamp. The hollow tip fibers were inserted into the dish approximately halfway and submerged to half the depth. Laser energy was delivered into the water and videos of particle flow were recorded under magnification at 10 fps. The recorded particle flow was used to map the flow of water for each fiber tip. Average velocities for the microspheres along the optical axis were observed qualitatively.

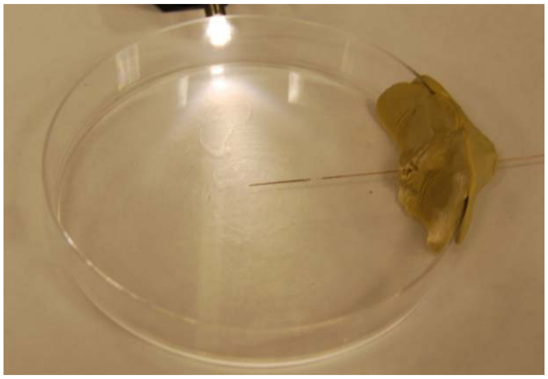

Figure 5.4: Petri dish (empty) with hollow fiber tip and side illumination.

5.2.3: Stone Ablation Study

The stone ablation performance of the hollow fiber tips were compared to a bare fiber, similar to chapter 4. Initial dry COM urinary stone mass was recorded with an analytical balance before securing the stone in place with a clamp and then submerging it into a saline bath (Figure 4.7). The laser radiation was delivered through the hollow fiber tips and bare fiber to the stone surface in contact mode. The fiber was held manually and a scanning motion over the stone surface under gentle force was used during pulsing to keep the fiber in contact with the stone's surface. A total of 9000 pulses was delivered to each stone sample, equivalent to stone ablation for 1 minute at 150 Hz. The stones were then dried in an oven at 70°C for over 30 minutes before final dry mass measurements were conducted. Optical transmission in air of each fiber including the bare fiber was ~ 90%, tested at a pulse rate of 10 Hz. Operating the hollow fiber tips at 150 Hz in air resulted in the stainless steel tube becoming "red hot." However, this effect was never observed when operating in saline or water. An output pulse energy of ~ 34 mJ was used with all fibers. A pulse rate of 150 Hz was chosen because fiber tip degradation appeared to become significant above ~ 100 Hz during the previous detachable tip study using a 300 μm core tip. The primary goal of the hollow fiber tips is to reduce degradation using small diameter fiber tips while maintaining high stone ablation rates.

5.2.4: Fiber Burn-back and Degradation

After stone ablation, a tiny wire was inserted into the distal opening of the hollow fiber tips and the distance traveled was measured as the overall fiber burn-back distance. The bare fiber was physically marked before and after and burn-back was measured using photography. A microscope was also used to image the fiber surfaces for degradation.

5.3: Results

5.3.1: Stone Ablation

Table 5.1 shows the average stone ablation rates for the four hollow tips tested and the bare fiber. The ablation rates measured were comparable to those reported previously with a bare 200 μm core fiber (~ 140 ± 35 μg/s at a pulse rate of 100 Hz) [44]. Average ablation rate appeared to decrease slightly with increasing fiber recession. A Student's t-test showed no statistical difference between the stone ablation rates for the bare fiber, and the fibers recessed 100 and 250 μm (t-test ≥ 0.8), or between 500 and 1000 μm (t-test ≥ 0.8). However, there was a statistical difference between the two groups (t-test ≤ 0.1).

Table 5.1: COM stone ablation rates and fiber burn-back for the hollow fiber tips as a function of fiber recession. Silica fiber with 150 μm core diameter. Rates calculated from mass loss after 9000 pulses at 150 Hz, 500 μs pulse duration (N≥5). Pulse energy: 34±1 mJ. Uncertainty of 25μm on burn-back measurements (N≥10).

Distance Recessed (μm)	Ablation Rate (μg/s)	Burn-back (μm/min)
0 (Bare Fiber)	194 ± 77	220
100	195 ± 48	0
250	188 ± 38	0
500	140 ± 52	0
1000	133 ± 46	0

Only the bare fiber showed overall fiber burn-back. No previous burn-back studies were found comparable to operating at a pulse rate of 150 Hz with the TFL. Flashing or sparking was witnessed during stone ablation with the all fibers. However, the frequency decreased with increasing fiber recession distance and it is unclear whether it originated from the stone or fiber. Lower bare fiber ablation rates may be due to the inconsistent tip geometry from burn-back or that the fiber tip is nearly invisible in saline and therefore was not in contact with the stone as frequent as the hollow fiber tips.

5.3.2: Fiber Tip Degradation

Microscopic imaging of the fiber tips provided different information than that of the fiber tip burn-back. The 100 and 250 µm recessed tips displayed similar degradation to that of the bare fiber, minus the overall fiber burn-back. At 500 µm a flat surface was still apparent, however a blistering or possibly roughened by dusting effect can be seen, indicating a partial phase change of the silica fiber. The fiber recessed 1 mm was the only fiber to still show a polished surface in most areas. The unpolished areas may be debris which could not be wiped off while the fiber is inside the hollow tip. The blurriness observed in the images could be attributed to the limited NA when imaging deep into the hollow tips with a high NA microscope.

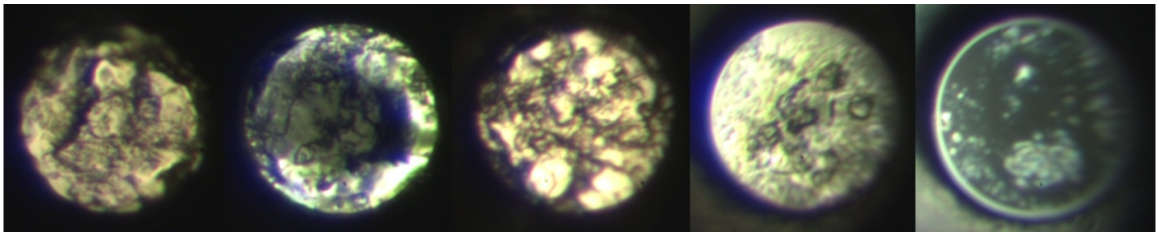
Bare Fiber 100 µm 250 µm 500 µm 1000 µm

Figure 5.5: Microscopic images of the hollow fiber tips compared to the bare fiber after 10 minutes at 150 Hz (90,000 total pulses). Decreasing tip degradation can be seen as fiber recession distance is increased.

A correlation was observed between the stone ablation rates and the fiber tip degradation, similar to the detachable fiber tip study. The stone ablation rates were divided into two statistically significant groups, which correlate with whether the fiber tip showed significant or minimal surface degradation.

5.3.3: Retropulsion

Particle velocities along the optical axis were observed at the beginning of laser operation, because after a few seconds a vortex was created by the limited volume of the Petri dish. Figure 5.6 shows representative images of the particle flow. The cavitation bubble is believed to be the cloudy cone-like shape at the fiber tip.

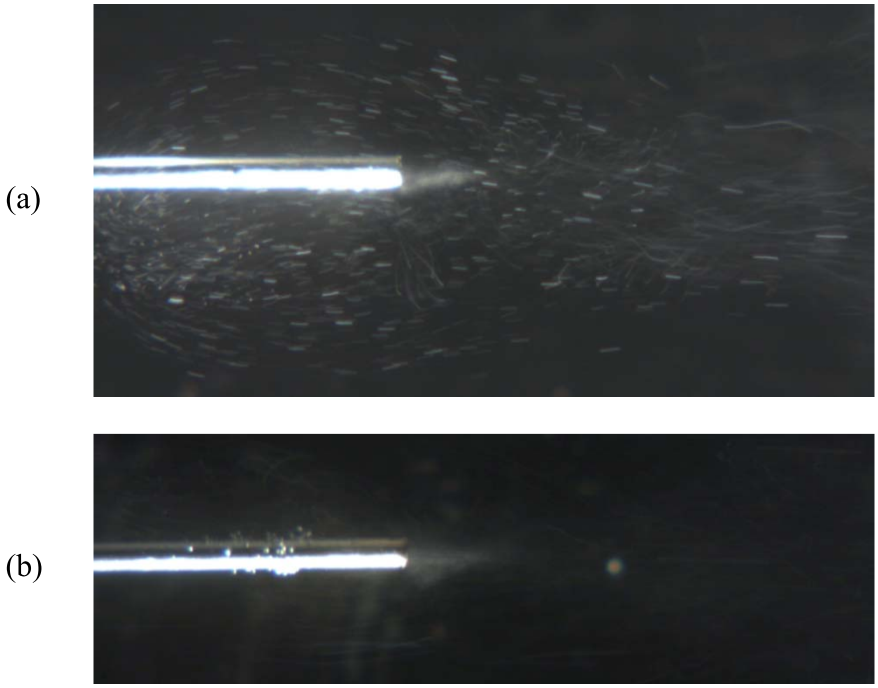

Figure 5.6: Hollow fiber tip with fiber recessed (a) 100 and (b) 1000 μm operating at 150 Hz. Velocity was observed to increase along the optical axis with deeper fiber recession, and with increasing pulse rate.

The speed of the microspheres in front of the fiber were too great to quantify with our imaging setup. Therefore, only a qualitative visual observation of increasing velocity can be stated for increasing fiber recession depth and for increasing pulse rate. It is unclear whether the bare fiber created more forward water flow than the 100 μm recessed fiber, however an increase can be seen when increasing the recessed distance to 1 mm.

5.4: Discussion

Use of hollow fiber tips instead of a bare fiber did not show a significant change in average stone ablation rate, which appeared to decrease only slightly with increasing fiber recession. Statistic analysis showed no difference between the bare fiber and a fiber recessed 250 µm, and only a drop to ~ 2/3 ablation rate for a fiber recession of 1 mm, the equivalent of a decrease in pulse rate of 2/3 for a bare fiber. The decrease in stone ablation rate for 500 and 1000 µm could be attributed to the diverging fiber output reflecting off the inner surface of the stainless steel tube, which is unpolished.

The advantage of using a hollow fiber tip is the minimal overall burn-back of the fiber tip. Some fiber tip surface degradation was noticed on fibers down to a recession depth of 250 µm, and the fiber at 1 mm still showed a polished surface after 90,000 pulses at 150 Hz. However, no recessed fibers lost their cladding or suffered from burn-back. Similar to the tapered fiber tip degradation observed in the previous chapter, the outer rim of the steel tube provided sufficient stone offset distance to prevent burn-back.

A potential disadvantage to using hollow fiber tips is the observed effect of increased forward water flow which may lead to increased stone retropulsion. An increase in particle velocity was observed with an increase in fiber recession depth. One possible cause of this effect may be that the cavitation bubble does not collapse back inside the hollow tip after the initial pulse and that this region remains a vapor pocket during laser operation. This vapor exerts a pressure which increases in the forward direction as the pocket increases along the same axis.

5.5: Integration with Stone Basket

Stone baskets have been used to assist ureteroscopic procedures for years by expanding at the stone site then collapsing around the stone for removal. In the case of laser lithotripsy, recent advances have been made to combine the laser operation with grasping the stone in a basket. Since the clinical laser used is still the Ho:YAG, the fibers used have core diameters greater than 200 μm and are disposable due to proximal and distal fiber tip damage. Figure 5.7 illustrates a commercial stone basket with outer diameter of 1.9 Fr or ~ 625 μm designed to be operated side-by-side with a laser lithotripsy fiber in the ureteroscope's working channel (~ 1 mm).

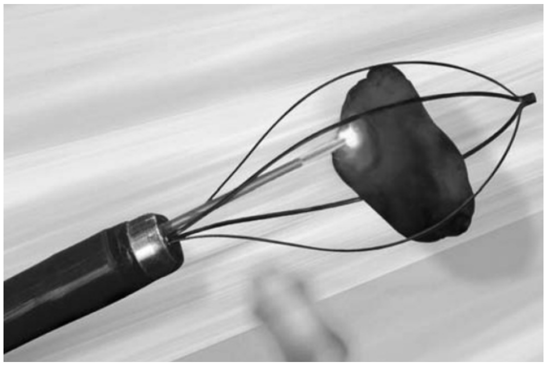

Figure 5.7: Simultaneous Ho:YAG lithotripsy using a 200 μm core diameter fiber of a calculus can occur while the calculus is entrapped within the Escape™ nitinol stone retrieval basket. Courtesy of Boston Scientific, Natick, MA [55].

Using the TFL, the hollow tip fibers could be integrated permanently into the same instrument. The hollow fiber tips would not suffer burn-back like standard fibers and therefore independent fiber manipulation would not be necessary, possibly reducing instrument cross-section. The stone basket may just collapse, as the stone shrinks due to ablation and fragmentation, keeping the stone in contact with the hollow fiber tip.

5.6: Fiber Muzzle

5.6.1: Theory and Motivation

The cavitation bubble formed in front of a fiber in aqueous medium has been studied for the past few decades [50, 56-65]. With a high speed camera the rapid expansion and collapse may be observed on the order of a few microseconds. Depending on the wavelength and pulse duration, these bubbles may take on many shapes. The pulse rate and pulse energy can affect the macroscopic region around the bubble, i.e. causing stone retropulsion.

The rapid expansion of hot gas at the distal tip has been studied for years in the firearms industry. In the case of a firearm, the explosive propellant gas, that follows the projectile, is diverted once the projectile leaves the barrel. The "muzzle" can divert the gas in a controllable manor, providing recoil reduction of the firearm. A cavitation bubble at the tip of an optical fiber could be treated in the same way.

A prototype fiber muzzle was created by drilling an ~ 350 μm hole near the tip of a 439 μm inner and 643 μm outer diameter stainless steel hypodermic tube. This tube was then positioned over a tube with an inner and outer diameter of 178 and 356 μm, respectively. The same tube was used for the hollow fiber tips in this chapter, however this time the fiber tip pretruded from the smaller tube and was positioned near the center of the through hole in the outer tube (Figure 5.8b). The fixed sides of the steel muzzle limit bubble expansion in that direction, while allowing only expansion out of the openings. The fiber position for the prototype was fixed with super glue at a recession distance of ~ 750 μm. Figure 5.8a shows the glued fiber muzzle prototype.

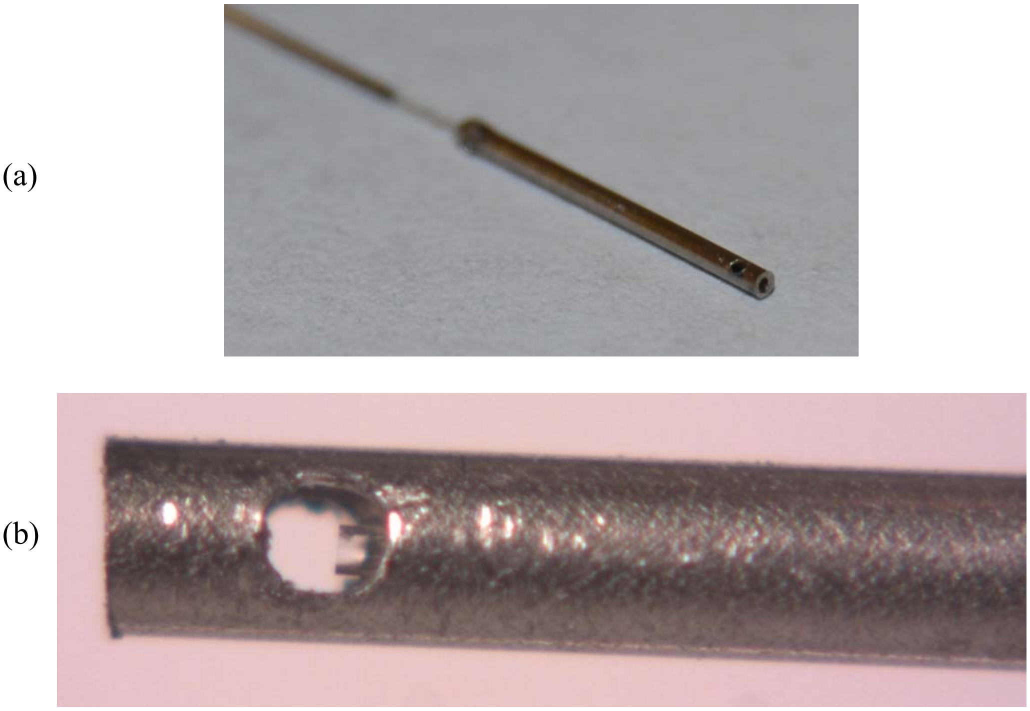

Figure 5.8: (a) Fiber muzzle attached to a 150 µm core diameter optical fiber, to control cavitation bubble expansion or retropulsion. Fiber is recessed 750 µm from distal end. Through hole diameter of ~ 350 µm and outer diameter of 643 µm. (b) Magnified image.

5.6.2: Prototype Testing

The fiber muzzle prototype was tested using the same procedures as the hollow fiber tips. Stone ablation occured at 34 mJ, 150 Hz pulse rate, and 500 µs pulse duration. However, the stone ablation rate was ~ 20 µg/s, well below the hollow fiber tips or bare fiber. This was believed to be a result of attenuation and stall out of the energy over a distance of 750 µm. Unlike the hollow fiber tips, the cavitation bubble was able to collapse back on the fiber tip and therefore acted similar to a bare fiber at a working distance of 750 µm from the stone.

However, by analyzing retopulsion or particle velocimetry a significant change was observed. A lesser forward flow was observed, along with significant perpendicular jet flow out of both holes in the muzzle (Figure 5.9).

Figure 5.9: Fiber muzzle submerged in a water bath with suspended microspheres. Perpendicular water flow can be seen exiting the holes in the muzzle. (a) Muzzle through hole oriented horizontal. (b) Vertical.

It is unclear how this particular prototype's flow might function inside a tight tube like the ureter. Figure 5.9b might be a more realistic model since the side flow almost immediately hits a barrier causing a chaotic flow pattern. However, with further exploration and computational fluid dynamic modelling of various designs the fiber muzzle could produce benefits to lithotripsy possibly counteracting retropulsion by creating a net reverse flow in the ureter while still ablating the stone.

5.7: Conclusions

This chapter introduced a novel design for a hollow fiber tip for potential use in thulium fiber laser lithotripsy. A simple hollow steel tube placed over a recessed and fixed fiber tip reduced or eliminated fiber tip degradation while still maintaining acceptable stone ablation rates and a small diameter footprint. Average stone ablation rates appeared to decrease slightly with increasing fiber recession, but only by a factor of 1/3 for a 1 mm recessed fiber. No overall burn-back was observed for all of the hollow fiber tips tested compared to over 200 µm a minute for a bare fiber. Some tip surface degradation was noticed on fibers down to a recession depth of 250 µm, and the fiber at 1 mm still showed a polished surface after 90,000 pulses at 150 Hz. A potential disadvantage to using hollow fiber tips is the observed effect of increased forward water flow or retropulsion. However, the hollow tip fibers could be integrated permanently into a stone isolation basket. A fiber muzzle was also introduced as a potential method for controlling retropulsion during laser lithotripsy. Hollow fiber tips are simple and inexpensive and could have an immediate and positive impact on laser lithotripsy.

CHAPTER 6: CONCLUSIONS

Laser energy coupled into an optical fiber can be delivered almost anywhere within the body to perform therapeutic surgery. Specialty fiber optic tips may provide increased precision and performance for certain applications in ophthalmology, oncology and urology. Chapter 2 demonstrated the design and performance of a mid-IR microsphere scalpel for potential use in proliferative diabetic retinopathy. Small single pulse ablation craters, less than 50 μm width and 20 μm depth were created in cornea tissue demonstrating the precision needed to potentially remove small deposits without damaging the underlying retina. Chapter 3 introduced improvements to the microsphere scalpel by creating the optimal device geometry that had only been modeled previously. This identical diameter sphere chain showed a self-limiting mechanism for ablation depth using chains of five spheres. Integration with other surgical tools including illumination, suction and a method for making the microsphere scalpel tip detachable and replaceable between surgical procedures was also determined. With further development, this novel approach to mid-IR laser ablation may provide an alternative to mechanical tools for surgical dissection and removal of ophthalmic tissues.

The current clinical laser lithotripter, the Holmium:YAG laser, cannot efficiently couple laser energy into small core diameter fibers without proximal fiber tip damage and therefore ureteroscope flexibility and irrigation are reduced. However, the Thulium fiber laser has recently been proposed as an alternative because its energy can be coupled into smaller diameter fibers, with no proximal fiber tip damage. With the risk of fiber damage contained at the distal tip, chapter 4 introduces an approach for using detachable fiber tips. A novel, low-profile (less than 1 mm outer diameter), spring-loaded, twist-locking, detachable distal fiber tip interface was designed, constructed, and tested *ex vivo* on urinary stones in the laboratory. Comparable stone ablation rates to previous TFL lithotripsy studies were observed. The highest ablation rates observed also contributed to the fastest distal fiber tip degradation, providing a motivation for urologists that desire shorter lithotripsy procedures to incorporate detachable distal fiber tips. Chapter 5 introduced a novel design for a hollow fiber tip for potential use in thulium fiber laser lithotripsy. An inexpensive and simple hollow steel tube placed over a recessed and fixed fiber tip reduced or eliminated fiber tip degradation while still maintaining acceptable stone ablation rates and a small diameter footprint. A potential disadvantage to using hollow fiber tips is the observed effect of increased stone retropulsion which could be counteracted by permanently integrating the hollow tip fibers into a stone isolation basket. All designs and devices shown were conceived to improve upon current surgical procedures and to reduce overall costs.

REFERENCES

[1] J. H. Kempen, B. J. O'Colmam, C. Leske *et al.*, “The prevalence of diabetic retinopathy among adults in the United States,” Archives of Ophthalmology*,* 122(4), 552-563 (2004).

[2] J. M. Krauss, and C. A. Puliafito, “Lasers in ophthalmology,” Lasers Surg Med*,* 17(2), 102-59 (1995).

[3] G. L. Spaeth, [Ophthalmic surgery, principles and practice] Saunders, Philadelphia(1982).

[4] J. W. Berger, and D. J. D'Amico, “Modeling of erbium: YAG laser-mediated explosive photovaporization: implications for vitreoretinal surgery,” Ophthalmic surgery and lasers*,* 28(2), 133-139 (1997).

[5] T. S. Alster, and J. R. Lupton, “Erbium:YAG cutaneous laser resurfacing,” Dermatologic clinics*,* 19(3), 453-466 (2001).

[6] R. Kaufmann, “Role of Erbium:YAG laser in the treatment of aged skin,” Clinical and Experimental Dermatology*,* 26(7), 631-636 (2001).

[7] P. Rechmann, D. S. Goldin, and T. Hennig, “Er:YAG lasers in dentistry: an overview,” 2-13 (1998).

[8] D. M. Clarkson, “A review of technology and safety aspects of erbium lasers in dentistry,” Dent Update*,* 28(6), 298-302 (2001).

[9] R. A. Hill, G. Baerveldt, S. A. Ozler *et al.*, “Laser trabecular ablation (LTA),” Lasers in Surgery and Medicine*,* 11(4), 341-346 (1991).

[10] S. A. Ozler, R. A. Hill, J. J. Andrews *et al.*, “Infrared laser sclerostomies,” Invest Ophthalmol Vis Sci*,* 32(9), 2498-503 (1991).

[11] M. L. McHam, D. L. Eisenberg, J. S. Schuman *et al.*, “Erbium: Yag Laser Trabecular Ablation with a Sapphire Optical Fiber,” Experimental Eye Research*,* 65(2), 151-155 (1997).

[12] P. D. Brazitikos, D. J. D'Amico, T. W. Bochow *et al.*, “Experimental ocular surgery with a high-repetition-rate erbium:YAG laser,” Invest Ophthalmol Vis Sci*,* 39(9), 1667-75 (1998).

[13] G. Stevens, Jr., B. Long, J. M. Hamann *et al.*, “Erbium:YAG laser-assisted cataract surgery,” Ophthalmic Surg Lasers*,* 29(3), 185-9 (1998).

[14] C. C. Neubaur, and G. Stevens Jr, "Erbium:YAG laser cataract removal: Role of fiber-optic delivery system," Journal of Cataract & Refractive Surgery, 25(4), 514-520 (1999).

[15] T. Wesendahl, P. Janknecht, B. Ott *et al.*, "Erbium: YAG laser ablation of retinal tissue under perfluorodecaline: determination of laser-tissue interaction in pig eyes," Invest Ophthalmol Vis Sci, 41(2), 505-12 (2000).

[16] U. Hohenleutner, S. Hohenleutner, W. Bäumler *et al.*, "Fast and effective skin ablation with an Er:YAG laser: Determination of ablation rates and thermal damage zones," Lasers in Surgery and Medicine, 20(3), 242-247 (1997).

[17] J. T. Walsh, T. J. Flotte, and T. F. Deutsch, "Er:YAG laser ablation of tissue: Effect of pulse duration and tissue type on thermal damage," Lasers in Surgery and Medicine, 9(4), 314-326 (1989).

[18] D. J. D'Amico, M. S. Blumenkranz, M. J. Lavin *et al.*, "Multicenter clinical experience using an erbium:YAG laser for vitreoretinal surgery," Ophthalmology, 103(10), 1575-85 (1996).

[19] D. J. D'Amico, P. D. Brazitikos, G. R. Marcellino *et al.*, "Initial clinical experience with an erbium:YAG laser for vitreoretinal surgery," American journal of ophthalmology, 121(4), 414-425 (1996).

[20] H. Hoerauf, A. Brix, C. Scholz *et al.*, "[Retinal photoablation with the Erbium:YAG laser. Initial experimental results for traction-free removal of tissue]," Ophthalmologe, 100(2), 115-21 (2003).

[21] M. H. Krause, and D. J. D'Amico, "Ablation of vitreous tissue with a high repetition rate erbium:YAG laser," Eur J Ophthalmol, 13(5), 424-32 (2003).

[22] D. P. Joseph, P. Allen, D. Negus *et al.*, "A new and improved vitreoretinal erbium:YAG laser scalpel: long-term morphologic characteristics of retinal-choroidal injury," Ophthalmic Surg Lasers Imaging, 35(4), 304-15 (2004).

[23] H. Hoerauf, A. Brix, J. Winkler *et al.*, "Photoablation of inner limiting membrane and inner retinal layers using the Erbium:YAG-laser: An in vitro study," Lasers in Surgery and Medicine, 38(1), 52-61 (2006).

[24] G. M. Hale, and M. R. Querry, "Optical-constants of water in 200-nm to 200-Mm wavelength region," Applied Optics, 12(3), 555-563 (1973).

[25] R. M. Verdaasdonk, and C. Borst, "Ray tracing of optically modified fiber tips. 1: spherical probes," Appl. Opt., 30(16), 2159-2171 (1991).

[26] K. Iwai, Y.-W. Shi, M. Endo *et al.*, "Penetration of High-Intensity Er:YAG Laser Light Emitted by IR Hollow Optical Fibers with Sealing Caps in Water," Appl. Opt., 43(12), 2568-2571 (2004).

[27] T. Watanabe, and Y. Matsuura, “Side-firing sealing caps for hollow optical fibers,” Lasers in Surgery and Medicine*,* 38(8), 792-797 (2006).

[28] D. X. Hammer, G. D. Noojin, R. J. Thomas *et al.*, “Intraocular laser surgical probe for membrane disruption by laser-induced breakdown,” Appl. Opt.*,* 36(7), 1684-1693 (1997).

[29] A. M. Kapitonov, and V. N. Astratov, “Observation of nanojet-induced modes with small propagation losses in chains of coupled spherical cavities,” Opt. Lett.*,* 32(4), 409-411 (2007).

[30] S. Yang, and V. N. Astratov, “Photonic nanojet-induced modes in chains of size-disordered microspheres with an attenuation of only 0.08dB per sphere,” Applied Physics Letters*,* 92(26), 261111 (2008).

[31] A. Darafsheh, A. Fardad, N. M. Fried *et al.*, “Contact focusing multimodal microprobes for ultraprecise laser tissue surgery,” Opt. Express*,* 19(4), 3440-3448 (2011).

[32] L. A. Remington, [Clinical Anatomy of the Visual System] Elsevier Butterworth Heinemann, Philadelphia, PA(2005).

[33] J. A. Harrington, “A Review of IR Transmitting, Hollow Waveguides,” Fiber and Integrated Optics*,* 19(3), 211-227 (2000).

[34] F. M. Recchia, I. U. Scott, G. C. Brown *et al.*, “Small-gauge pars plana vitrectomy: a report by the American Academy of Ophthalmology,” Ophthalmology*,* 117(9), 1851-7 (2010).

[35] J. Y. Clark, I. M. Thompson, and S. A. Optenberg, “Economic Impact of Urolithiasis in the United States,” The Journal of urology*,* 154(6), 2020-2024 (1995).

[36] G. J. Vassar, K. F. Chan, J. M. Teichman *et al.*, “Holmium: YAG lithotripsy: photothermal mechanism,” J Endourol*,* 13(3), 181-90 (1999).

[37] S. Griffin, "Fiber optics for destroying kidney stones." 11, 44-47.

[38] A. J. Marks, A. C. Mues, B. E. Knudsen *et al.*, “Holmium:yttrium-aluminum-garnet lithotripsy proximal fiber failures from laser and fiber mismatch,” Urology*,* 71(6), 1049-51 (2008).

[39] B. E. Knudsen, R. Pedro, B. Hinck *et al.*, “Durability of reusable holmium:YAG laser fibers: a multicenter study,” J Urol*,* 185(1), 160-3 (2011).

[40] N. M. Fried, “Thulium fiber laser lithotripsy: an in vitro analysis of stone fragmentation using a modulated 110-watt Thulium fiber laser at 1.94 microm,” Lasers Surg Med*,* 37(1), 53-8 (2005).

[41] N. J. Scott, C. M. Cilip, and N. M. Fried, "Thulium Fiber Laser Ablation of Urinary Stones Through Small-Core Optical Fibers," Ieee Journal of Selected Topics in Quantum Electronics, 15(2), 435-440 (2009).

[42] R. L. Blackmon, P. B. Irby, and N. M. Fried, "Holmium:YAG (lambda = 2,120 nm) versus thulium fiber (lambda = 1,908 nm) laser lithotripsy," Lasers Surg Med, 42(3), 232-6 (2010).

[43] R. L. Blackmon, P. B. Irby, and N. M. Fried, "Thulium fiber laser lithotripsy using tapered fibers," Lasers Surg Med, 42(1), 45-50 (2010).

[44] R. L. Blackmon, P. B. Irby, and N. M. Fried, "Comparison of holmium:YAG and thulium fiber laser lithotripsy: ablation thresholds, ablation rates, and retropulsion effects," J Biomed Opt, 16(7), 071403 (2011).

[45] R. L. Blackmon, P. B. Irby, and N. M. Fried, "Enhanced thulium fiber laser lithotripsy using micro-pulse train modulation," J Biomed Opt, 17(2), 028002 (2012).

[46] K. T. Schomacker, Y. Domankevitz, T. J. Flotte *et al.*, "Co:MgF2 laser ablation of tissue: effect of wavelength on ablation threshold and thermal damage," Lasers Surg Med, 11(2), 141-51 (1991).

[47] E. D. Jansen, T. G. van Leeuwen, M. Motamedi *et al.*, "Temperature dependence of the absorption coefficient of water for midinfrared laser radiation," Lasers Surg Med, 14(3), 258-68 (1994).

[48] B. I. Lange, T. Brendel, and G. Huttmann, "Temperature dependence of light absorption in water at holmium and thulium laser wavelengths," Applied Optics, 41(27), 5797-5803 (2002).

[49] A. Vogel, P. Schmidt, and B. Flucke, "Minimization of thermomechanical side effects in IR ablation by use of multiple q-switched laser pulses," Medical Laser Applications, 17(1), 15-20 (2002).

[50] M. Frenz, F. Konz, H. Pratisto *et al.*, "Starting mechanisms and dynamics of bubble formation induced by a Ho : Yttrium aluminum garnet laser in water," Journal of Applied Physics, 84(11), 5905-5912 (1998).

[51] B. E. Knudsen, R. D. Glickman, K. J. Stallman *et al.*, "Performance and safety of holmium: YAG laser optical fibers," J Endourol, 19(9), 1092-7 (2005).

[52] A. C. Mues, J. M. Teichman, and B. E. Knudsen, "Quantification of holmium:yttrium aluminum garnet optical tip degradation," J Endourol, 23(9), 1425-8 (2009).

[53] N. J. Scott, R. A. Barton, A. L. Casperson *et al.*, "Mid-IR germanium oxide fibers for contact erbium laser tissue ablation in endoscopic surgery," Ieee Journal of Selected Topics in Quantum Electronics*,* 13(6), 1709-1714 (2007).

[54] R. L. Blackmon, J. R. Case, S. R. Trammell *et al.*, "Fiber-optic manipulation of urinary stone phantoms using holmium:YAG and thulium fiber lasers," Journal of Biomedical Optics*,* 18(2), 028001-028001 (2013).

[55] S. S. Kesler, S. A. Pierre, D. I. Brison *et al.*, "Use of the Escape nitinol stone retrieval basket facilitates fragmentation and extraction of ureteral and renal calculi: a pilot study," J Endourol*,* 22(6), 1213-7 (2008).

[56] A. Vogel, "Acoustic transient generation by laser-produced cavitation bubbles near solid boundaries," The Journal of the Acoustical Society of America*,* 84(2), 719 (1988).

[57] T. Asshauer, K. Rink, and G. Delacretaz, "Acoustic Transient Generation by Holmium-Laser-Induced Cavitation Bubbles," Journal of Applied Physics*,* 76(9), 5007-5013 (1994).

[58] P. Zhong, H. L. Tong, F. H. Cocks *et al.*, "Transient cavitation and acoustic emission produced by different laser lithotripters," J Endourol*,* 12(4), 371-8 (1998).

[59] C. D. Ohl, T. Kurz, R. Geisler *et al.*, "Bubble dynamics, shock waves and sonoluminescence," Philosophical Transactions of the Royal Society of London Series a-Mathematical Physical and Engineering Sciences*,* 357(1751), 269-294 (1999).

[60] K. F. Chan, T. J. Pfefer, J. M. Teichman *et al.*, "A perspective on laser lithotripsy: the fragmentation processes," J Endourol*,* 15(3), 257-73 (2001).

[61] E. A. Brujan, G. S. Keen, A. Vogel *et al.*, "The final stage of the collapse of a cavitation bubble close to a rigid boundary," Physics of Fluids*,* 14(1), 85-92 (2002).

[62] E. A. Brujan, and A. Vogel, "Stress wave emission and cavitation bubble dynamics by nanosecond optical breakdown in a tissue phantom," Journal of Fluid Mechanics*,* 558, 281-308 (2006).

[63] E. Fuh, G. E. Haleblian, R. D. Norris *et al.*, "The effect of frequency doubled double pulse Nd:YAG laser fiber proximity to the target stone on transient cavitation and acoustic emission," J Urol*,* 177(4), 1542-5 (2007).

[64] T. Lu, Q. Xiao, D. Xia *et al.*, "Cavitation effect of holmium laser pulse applied to ablation of hard tissue underwater," J Biomed Opt*,* 15(4), 048002 (2010).

[65] B. Han, Y. X. Pan, Y. L. Xue *et al.*, “Mechanical effects of laser-induced cavitation bubble on different geometrical confinements for laser propulsion in water,” Optics and Lasers in Engineering*,* 49(3), 428-433 (2011).

APPENDIX A: PEER-REVIEWED PUBLICATIONS

[1] **Thomas C. Hutchens**, Arash Darafsheh, Vasily N. Astratov, Amir Fardad, Andrew N. Antoszyk, Howard S. Ying, and Nathaniel M. Fried, "Contact focusing multimodal probes for potential use in ophthalmic surgery with the Erbium:YAG laser," Journal of Biomedical Optics, in preparation.

[2] **Thomas C. Hutchens**, Richard L. Blackmon, William C. Perkins, Pierce B. Irby, and Nathaniel M. Fried, "Hollow fiber optic tips to reduce distal tip degradation during thulium fiber laser lithotripsy," Journal of Biomedical Optics, in preparation.

[3] **Thomas C. Hutchens**, Serhat Tozburun, Michael A. McClain, Gwen A. Lagoda, Arthur L. Burnett, and Nathaniel M. Fried, "Temperature controlled optical stimulation of the rat prostate cavernous nerves," Journal of Biomedical Optics, in preparation.

[4] Christopher M. Cilip, Sarah B. Rosenbury, Nicholas Giglio, **Thomas C. Hutchens**, Gino R. Schweinsberger, Duane E. Kerr, Cassandra Latimer, William H. Nau, Jr., and Nathaniel M. Fried, "Infrared laser sealing of blood vessels: preliminary ex vivo tissue studies," Journal of Biomedical Optics, in revision.

[5] **Thomas C. Hutchens**, Richard L. Blackmon, Pierce B. Irby, and Nathaniel M. Fried, "Detachable fiber optic tips for use in thulium fiber laser lithotripsy," Journal of Biomedical Optics, 18(3) March 2013.

[6] **Thomas C. Hutchens**, Arash Darafsheh, Vasily N. Astratov, Amir Fardad, Andrew N. Antoszyk, Howard S. Ying, and Nathaniel M. Fried. "Characterization of novel microsphere chain fiber optic tips for potential use in ophthalmic laser surgery," Journal of Biomedical Optics, 17(6) June 2012.

APPENDIX B: CONFERENCE PROCEEDINGS

[1] **Thomas C. Hutchens**, Richard L. Blackmon, Pierce B. Irby, and Nathaniel M. Fried, “Comparison of detachable and tapered fiber optic tips for use in thulium fiber laser lithotripsy,” Proc. SPIE 8565, 2013.

[2] **Thomas C. Hutchens** & Arash Darafsheh, Amir Fardad, Andrew N. Antoszyk, Howard S. Ying, Nathaniel M. Fried, and Vasily N. Astratov, “Contact focusing multimodal probes for potential use in ophthalmic surgery with the Erbium:YAG laser,” Proc. SPIE 8567, 2013.

[3] Christopher M. Cilip, Sarah B. Rosenbury, Nicholas Giglio, **Thomas C. Hutchens**, Gino R. Schweinsberger, Duane E. Kerr, Cassandra Latimer, William H. Nau, Jr., and Nathaniel M. Fried, “Thermal sealing of blood vessels using infrared lasers,” Proc. SPIE 8565, 2013.

[4] Serhat Tozburun, Charlotte D. Stahl, **Thomas C. Hutchens**, Gwen A. Lagoda, Arthur L. Burnett, and Nathaniel M. Fried, “Subsurface optical stimulation of rat prostate cavernous nerves using a continuous wave, single mode, 1490 nm diode laser,” Proc. SPIE 8565, 2013.

[5] Charlotte D. Stahl, Serhat Tozburun, **Thomas C. Hutchens**, Gwen A. Lagoda, Arthur L. Burnett, Matthew D. Keller, and Nathaniel M. Fried, “Comparison of three pulsed infrared lasers for optical stimulation of the rat prostate cavernous nerves,” Proc. SPIE 8565, 2013.

[6] **Thomas C. Hutchens**, Arash Darafsheh, Amir Fardad, Andrew N. Antoszyk, Howard S. Ying, Vasily N. Astratov, and Nathaniel M. Fried, “Novel microsphere chain fiber tips for use in mid-infrared ophthalmic laser surgery,” Proc. SPIE 8218, 2012.

[7] Arash Darafsheh, Anatole Lupu, S. A. Burand, **Thomas C. Hutchens**, Nathaniel M. Fried, and Vasily N. Astratov, “Photonic nanojet-induced modes: fundamentals and applications,” Proc. SPIE 8264, 2012.

APPENDIX C: PATENTS

[1] Nathaniel. M. Fried, Richard L. Blackmon, Pierce B. Irby, and **Thomas C. Hutchens**, "Novel endoscope tube with detachable fiber tips," Provisional U.S. patent filed, Application # 61/296,921, Jan. 2010.

APPENDIX D: ASSEMBLY OF GLUED MICROSPHERE SCALPEL

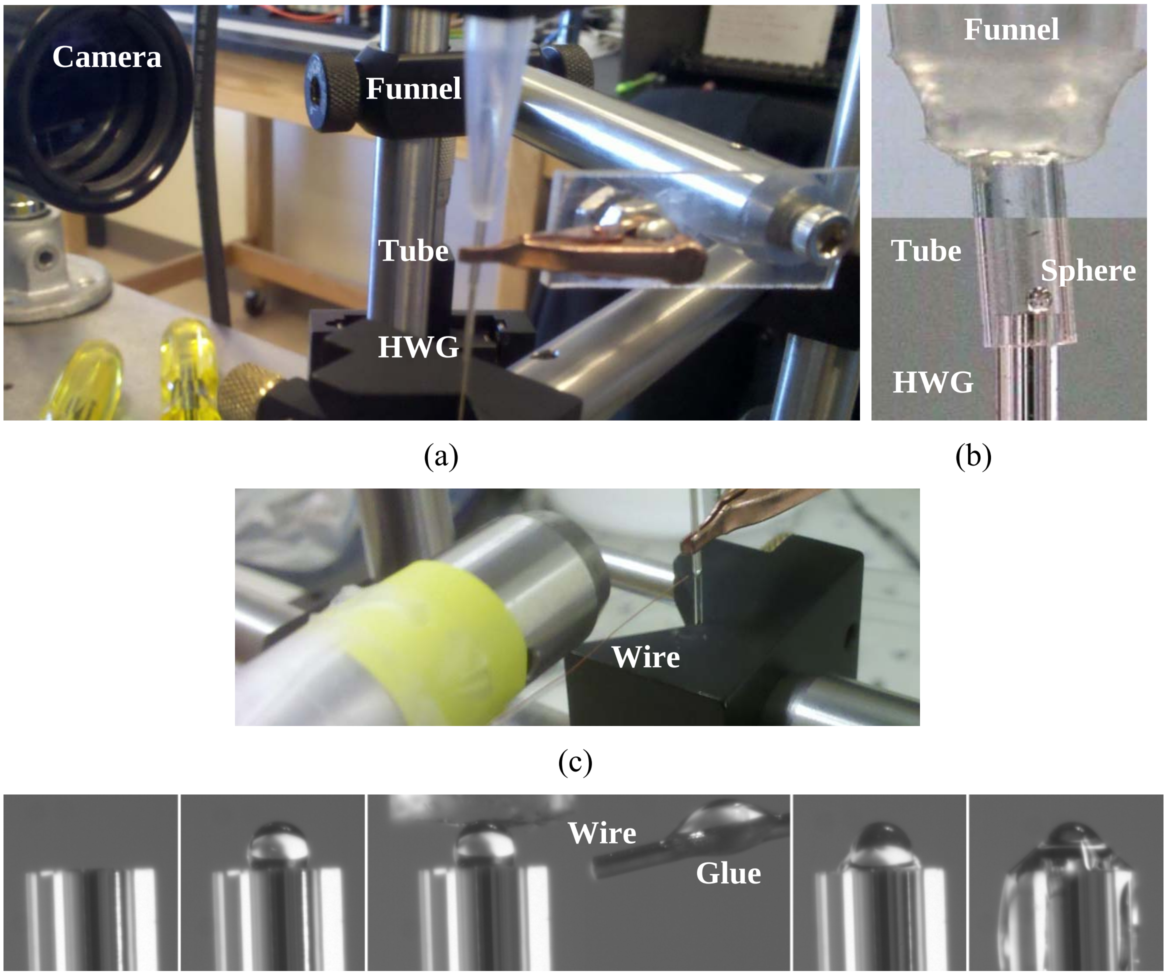

(a) (b)

(c)

(d)

(a) A funnel and tube guide the dropped sphere to the hollow waveguide
(b) Magnification by camera
(c) A small gauge wire, dipped in epoxy, is guided to the sphere by a micromanipulation stage
(d) Sphere is held in place during gluing by the guiding tube
Epoxy is then cured by UV lamp

APPENDIX E: ASSEMBLY OF LITHOTRIPSY DETACHABLE TIPS

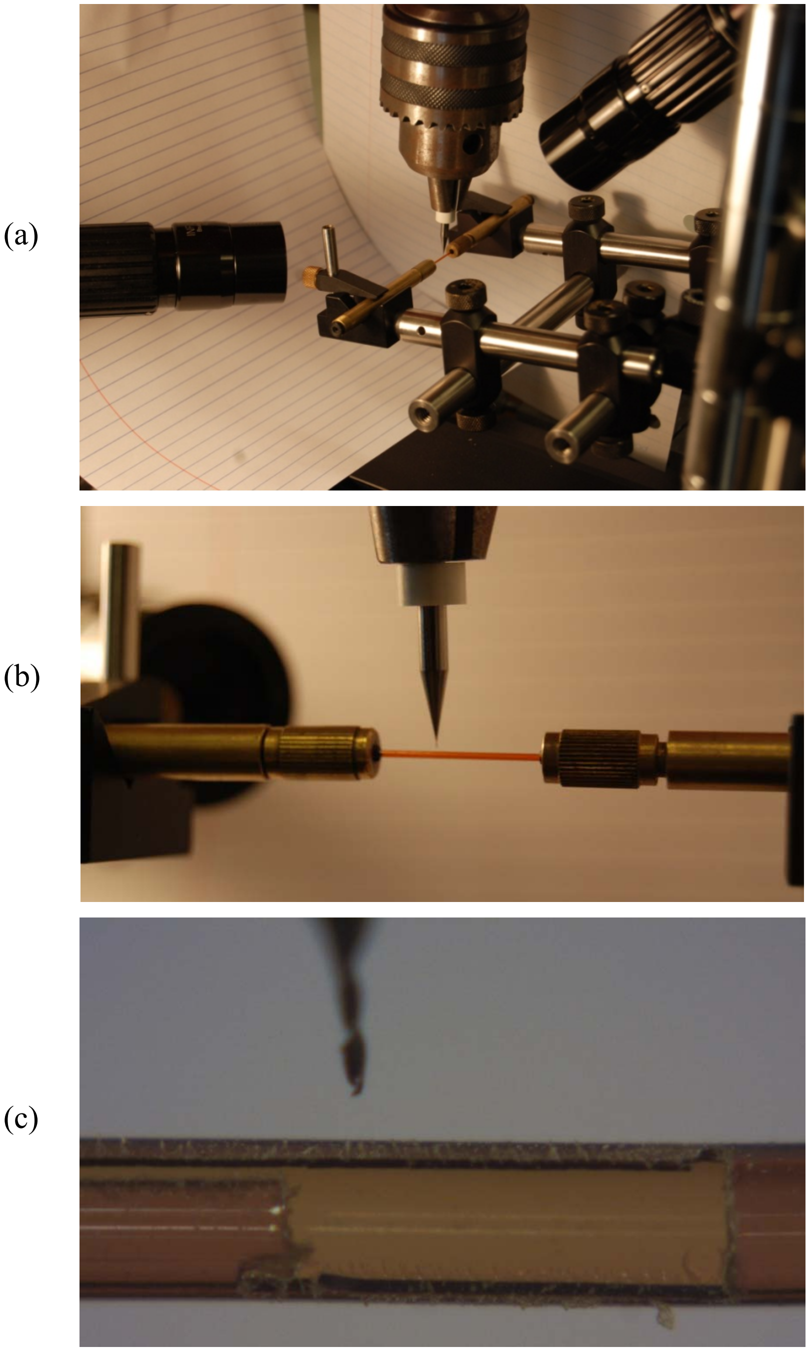

(a) Polyimide tubing held on both ends by fiber chucks underneath drill
(b) Magnified milling setup
(c) J-groove carved in polyimide tubing with 125 μm milling bit using micromanipulation stages

(d)

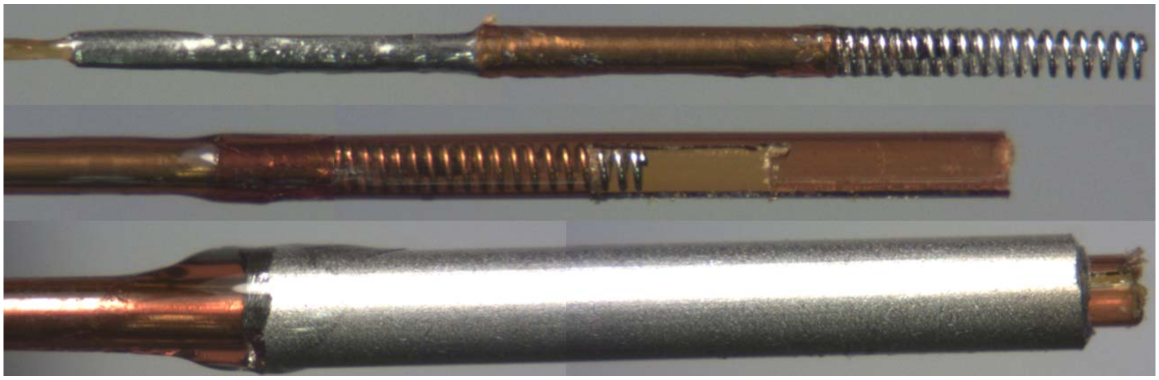

(e)

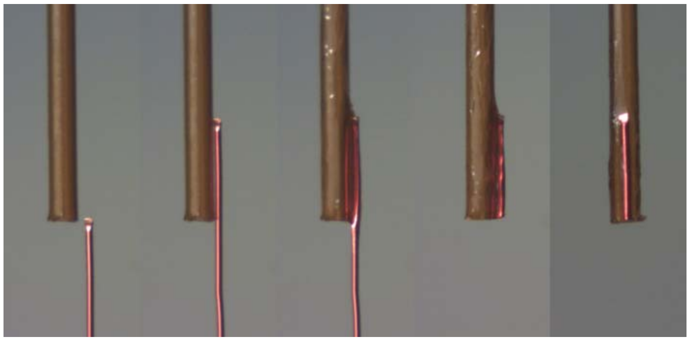

(f)

(g)

(h)

(d) Steel tubing counterbored with drill bit for easier fiber insertion
(e) Tubing, spring, J-groove, and outer cover glued over trunk fiber
(f) 36 gauge wire positioned adjacent to tip sleeve, glued and then cut
(g) Completed prototype detached (h) attached